

Lithographically-Scribed Planar Holographic Optical CDMA Devices and Systems  
A Phase II SBIR Contract: Final Report

February 15, 2007

Sponsored by:

Defense Advanced Research Projects Agency (DoD)  
U.S. Research, Development and Engineering Command (RDECOM)

ARPA Order Nr. 2913-14

Issued by: US Army Aviation & Missile Command Under  
Contract No. W31P4Q-05-C-R149

Contractor: LightSmyth Technologies, Inc.  
Principal Investigator: Dr. Thomas Mossberg, Ph.D.  
1720 Willow Creek Circle, Suite 520  
Eugene, OR 97402  
(541) 431-0026

Effective Date of Contract: 02 February 2005

Short Title of Work: Final Report

Contract Expiration Date: 02 February 2007  
Reporting Period: 02 February 2005 – 02 February 2007

Disclaimer: The views and conclusions contained in this document are those of the authors and should not be interpreted as representing the official policies, either express or implied, of the Defense Advanced Research Projects Agency or the U.S. Government.

Approved for public release; distribution unlimited.

## Table of Contents

|  |           |
|--|-----------|
| <b>Executive Summary.....</b>  | <b>3</b>  |
| <b>Introduction .....</b>  | <b>4</b>  |
| Phase II Single-mode CWDM mux Device .....   | 7         |
| Layout of Phase II Device .....  | 7         |
| Phase and Amplitude Apodization for Advanced Filter Design .....                                 | 8         |
| Achievable HBR reflective bandwidth .....  | 9         |
| Reflective Bandwidth – Single Mode Architecture.....   | 10        |
| Specifics of Multi-Mode Device Operation .....   | 10        |
| Reflective Bandwidth – Multi-Mode Architecture.....  | 14        |
| Overview of Phase II Objectives .....  | 14        |
| <b>Results of Phase II development .....</b>   | <b>15</b> |
| Design Strategy for HBR waveguides .....   | 15        |
| Initial multi-HBR device results .....   | 16        |
| First Realization of Low-Loss, Flat Passband Filtering Function .....                            | 18        |
| Preliminary 4-channel CWDM multiplexer/demultiplexer .....                                       | 20        |
| “Accordion” Apodization.....   | 22        |
| HBR Fabrication Process .....  | 24        |
| Product Level HBR multiplexer Performance.....   | 25        |
| Eight-Channel Multiplexer .....  | 25        |
| Four-channel apodized, high performance, integrated HBR mux .....                                | 26        |
| Split-Contour Apodization .....  | 29        |
| Chromatic Dispersion in HBR CWDM Multiplexers.....   | 32        |
| Impact of Waveguide Non-Uniformity .....   | 35        |
| Measurement .....  | 35        |
| Compensating device geometries.....  | 36        |
| Properties of HBR-based multiplexers in Silicon-on-Insulator Formats .....                       | 40        |
| Conclusions and Comparison: Multimode CWDM in SOI .....  | 46        |
| Structuring HBR Diffractive Contours To Minimize Wavefront Aberration .....                      | 46        |
| Replication of HBR devices in PMMA .....   | 47        |
| Packaging Of HBR Mux Devices .....   | 49        |
| Preparation of device die .....  | 49        |
| Optical alignment .....  | 51        |
| <b>References .....</b>  | <b>55</b> |
| <b>Appendix A (Specification Sheet for LightSmyth HBR-based CWDM 4-channel mux product).....</b> | <b>56</b> |
| <b>Appendix B (Specification Sheet for LightSmyth HBR-based CWDM 8-channel mux product).....</b> | <b>58</b> |

**Executive Summary:** Recent advances in photolithographic fabrication and planar waveguides have created a powerful opportunity. For the first time, it is possible to generate arbitrary computer-designed, waveguide, volume holograms and to do so robustly and at low cost. Holographic Bragg Reflectors (HBRs) comprise an exemplary lithographically scribed fully integrated holographic device useful for multiplexing of wavelength differentiated optical signals and general purpose spectral filtering. HBRs provide both a flexible spectral filtering function and a signal routing/imaging function in the slab waveguide environment. The present Phase II effort has harnessed new fabrication tools to perfect disruptive HBR-based multiplexer products for DoD avionics, optical communication systems, computer data communications and local area networks. The devices can address both single and multimode systems providing high levels of functionality and reliability at low cost. In multi-mode configuration, the devices may be used to enhance and retrofit the existing optical communication systems in aircraft and ships as well as empower powerful new cost effective solutions in both commercial and military data transport systems. HBR-based multiplexing is empowering to WDM-on-a-chip hybrid integration enabling compact, low-cost, high capacity optical transport specialized to small network environments. As a result of the present effort, the first fully integrated Course Wavelength Division Multiplexer compatible with single-mode systems and competitive with multiplexers constructed from discrete thin film filters has been developed and demonstrated. The silica-on-silicon format was employed. A multitude of methods for providing precisely tailored, flat passbands were successfully demonstrated. Design tools necessary to implement aspheric diffractive contours and thereby minimize imaging aberrations were developed. Fabrication yields were examined and factors limiting same identified. Structural modifications expected to improve yields were identified. Implementations of HBR multiplexers in multimode silicon-on-insulator were investigated and simulated. Replication of diffractive structures used in HBR devices was demonstrated in PMMA thereby demonstrating that the outlook on very low cost polymer-based multimode HBR multiplexers is very promising.

## Introduction

Technological development across fields is tightly interwoven. Profound technological opportunity in one field frequently arises from cumulative enabling developments in a variety of other fields. In the present instance, the area of technological and product opportunity relates generally to photonics and specifically to lithographically-scribed planar holographic photonic devices. Lithographically-scribed planar holographic devices (or integrated holographic devices) may be thought of as photonic transport and processing fabrics and offer powerful functionality in a number of areas as shown schematically by the single-chip mux/demux, source/receiver in Figure 1.

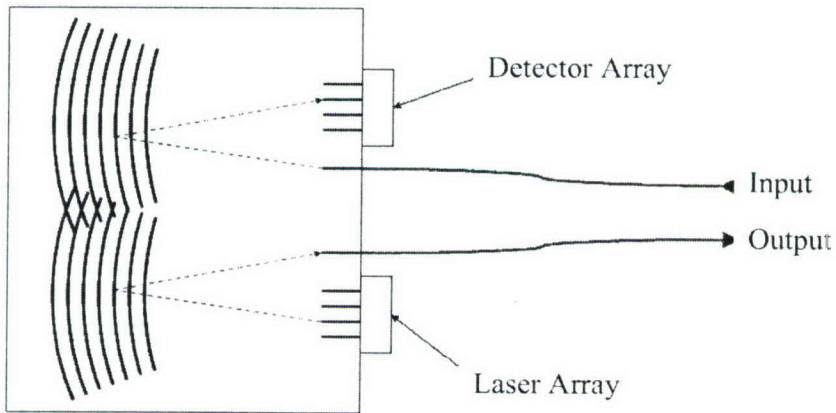


Figure 1. Schematic of a transmit/receive/mux unit based on slab waveguide holographic Bragg reflectors

Integrated holographic devices have been enabled through recent refinements in nanofabrication as utilized in electronics manufacture, planar waveguide technology, and advanced optical design concepts involving the interaction of optical signals with computer-designed volume holograms. Devices based on integrated holography address a number of product areas. The specific device whose development was undertaken in the present program, holographic Bragg reflectors (HBRs), comprise integrated multiplexers and demultiplexers for wave-division-multiplexed (WDM) communications systems utilizing wide-wavelength channel spacing (coarse WDM or CWDM) as are employed in data communications, local area nets, on DoD systems such as aircraft and ships, and in access-level telecommunications. HBR devices can address both single and multimode systems providing high levels of functionality and reliability at low cost. Also considered are hybrid integrated CWDM transmitters and receivers which couple the integrated HBR multiplexing technology with laser and detector arrays to form low-cost yet high performance WDM-enabling transmitter and receiver subsystems as shown in Figure 1. The HBR multiplexing devices are shown schematically at the left as the curved lines which would be etched onto a planar waveguide substrate. Such subsystems provide for the tractable expansion of existing DoD single-channel communication systems to higher capacity WDM systems without complete reinstallation.

Over the last few years, dramatic advances in lithography have accrued. It is now a routine matter to create centimeter-scale planar circuit structures with feature sizes on the 100 nanometer level. Feature sizes of 100-300 nm are required in order to implement general computer-generated holographic structures. Importantly for photonic applications, tests have revealed that electronic fabrication tools create spatially coherent structures. This means that the absolute placement of features is true to interferometric accuracy over fabricated structures up to distances of centimeter scale<sup>1</sup>. Achievement of such spatial coherence via standard electronics industry deep-ultraviolet (DUV) stepper-based fabrication tools now allows for low-cost, volume fabrication of photonic structures that could only have been dreamed of in prior years.

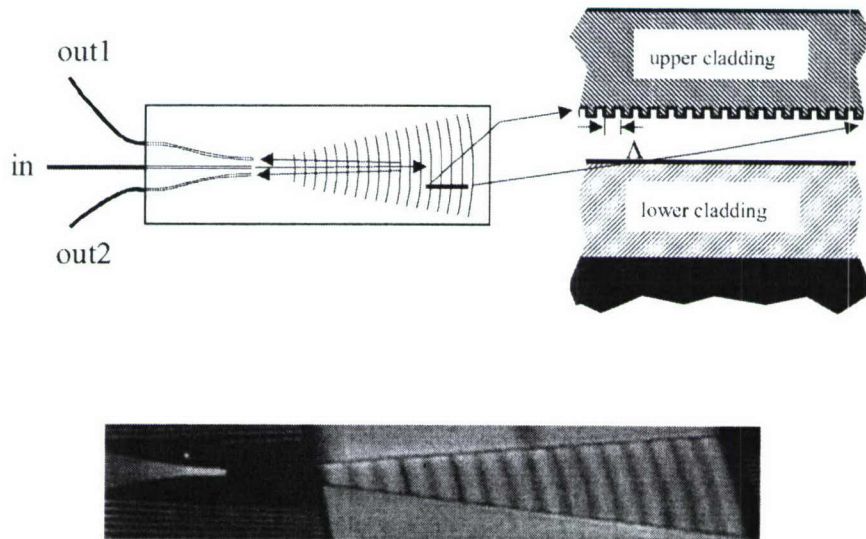


Figure 2. Top: schematic top view and cross section of a two-channel HBR slab waveguide filter. Bottom: photograph of a fabricated two-channel HBR slab waveguide filter.

Early on in this SBIR , LightSmyth designed, analyzed, and fabricated a test HBR device. This HBR device was designed to provide spectral and temporal coding of optical signals for Optical Code-Division Multiple Access (OCDMA) systems. In Figure 2, we show (clockwise from upper left) a schematic top view of the planar device, a schematic cut-away side view of the device, and a photograph of the actual fabricated device. The device is based on a silica-on-silicon slab waveguide structure with a core guiding layer sandwiched between two cladding layers. The upper surface of the core layer is etched according to a design pattern, which provides spectral filtering and wavefront shaping of the signals. The device fabricated has a single input port and two separate output ports. The spectral transfer function between the input and each of the outputs is different. Coupling between the input and each output is implemented

<sup>1</sup> Fourier-transform-limited performance of a lithographically scribed planar holographic Bragg reflector, Greiner, C.; Iazikov, D.; Mossberg, T.W., Photonics Technology Letters, IEEE 16, 840 (2004).

via separate HBR devices that spatially overlap throughout the pie-shaped footprint (2 cm total length).

During the initial SBIR work it was found that HBR devices could be fabricated in a spatially coherent manner using standard DUV photolithographic fabrication technology and that the spatial and spectral transfer functions of the devices could be accurately programmed through computer design of diffractive contour. Photolithographically scribed devices of such high spatial coherence had not previously been demonstrated. Neither had the precision computer-based design and fabrication of volume holographic functional elements requiring quarter-micron-scale spatial resolution.

The first focus of the Phase II SBIR work was a multiplexer for single-mode CWDM communication systems capable of enhancing performance in both DoD and commercial optical communication systems. Follow-on multimode versions of the product are enablers of retrofit upgrade of single-wavelength optical communication links to CWDM (without fiber re-installation), which is especially useful in the upgrade of existing DoD platforms. Single-mode versions of the product support new high capacity CWDM systems with superior operational specifications and cost/benefit figures. Successful introduction of the target product will provide a legitimization and financial basis for long-term development of the many and diverse products derivative to the core technology, which include filter arrays for real-time spectral target recognition, temporal waveform processing via cross-correlation with arrays of device-encoded reference waveforms, optical packet header recognition, distributed photonic transport fabrics for spatial-contention-free optical signal routing in integrated photonic circuits, true-time delay for RF photonics, and many other applications where the powerful spectral and spatial signal processing capabilities of planar holographic structures may be employed.

The HBR multiplexer developed in this program comprises a fully integrated, single-chip, device for coarsely spaced, wave-division multiplexed (or CWDM as described above) communication systems employed by DoD and the commercial market. The single-mode version was developed first because Phase I work had successfully demonstrated the key techniques. The multi-mode version, which is well-suited to provide an upgrade path for existing DoD airborne communications systems, has been partially developed in various formats including silica-on-silicon, silicon-on-insulator, and polymer. Based on the outstanding success achieved with the single-mode CWDM mux/demux units, it is anticipated that ultimate completion of the multi-mode mux/demux versions will be entirely tractable.

It should be noted that Dense WDM systems were designed for long-haul telecommunication systems wherein it was imperative that many wavelength differentiated signal channels could be amplified within the limited gain bandwidth of erbium-doped fiber amplifiers. Resulting DWDM systems have closely spaced channels. Communication systems employing closely spaced channels must be implemented with high precision optical components. High precision components are intrinsically high cost and have limited temperature and mechanical stability. Such systems, needed for long-haul communications, are poorly suited to local networks where amplification is unnecessary. HBR devices enable the implementation of WDM systems optimally designed for local network needs whether in a military aircraft or ship or in a commercial environment. Ultimate performance and cost advantage of WDM system optimized

for local networks will dramatically exceed levels provided by communication systems optimized for long-haul telecommunications application. It is important to move beyond the late '90's focus on long-haul telecommunications to systems optimized for other scenarios.

### Phase II Single-mode CWDM mux Device

As currently implemented, standard coarse WDM systems utilize a set of typically 16-18 wavelength channels. Channels are spaced by 20 nm and typically the passband for each channel is very flat over a passband width of 13 nm. The channel transfer function exhibits a rapid fall-off beyond the passband. Existing multiplexer/demultiplexer devices for this coarse WDM standard are typically assembled arrays of discrete thin film filters (TFF). High-end, single-mode, 8-channel, TFF-based coarse WDM multiplexers exhibit insertion loss (IL) of about 2.5 dB and insertion loss non-uniformity across 8 channels of about 1.3 dB. Our design objective was to produce a fully integrated device with competitive specifications. Additionally, we targeted performance at less than 0.3 dB polarization-dependent loss (PDL), adjacent channel isolation of 30 dB, and ability to operate in -40 to 85°C range without active thermal stabilization.

### Layout of Phase II Device

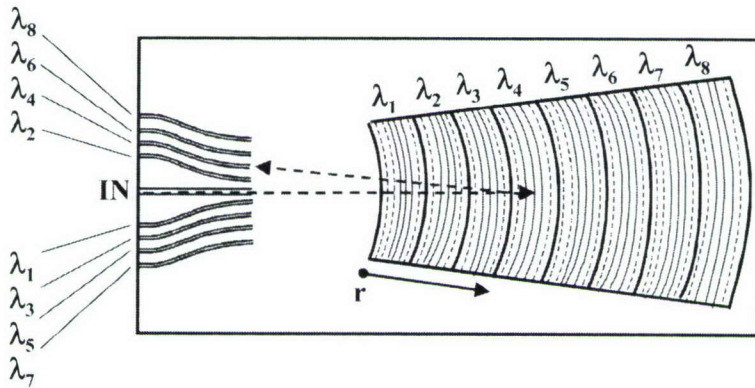


Figure 3. Schematic layout of 8-channel CWDM mux (silica-on-silicon) successfully developed.

Figure 3 gives a schematic top view picture of an integrated eight-channel lithographically scribed planar holographic demultiplexer prototyped and proven in the course of this SBIR work. Single-mode versions of the device are based on silica-on-silicon planar waveguides. Diffractive elements (the curved lines to the right of the Figure 3) are etched in the core waveguide layer and filled with cladding. An optical signal containing a plurality of wavelength channels enters the planar device through the IN port. Each one of the sections at right labeled by a distinct wavelength acts to back diffract one wavelength to a corresponding output port. Light emerging from the output ports consists of a single wavelength-delineated communication channel. Typically an optical detector is employed to monitor the output of each wavelength specific output channel. The device may be used in reverse as a multiplexer. In this case, the IN port becomes the OUT port and all signal directions are reversed. A photograph of a test die with various HBR multiplexers is shown in Figure 4.

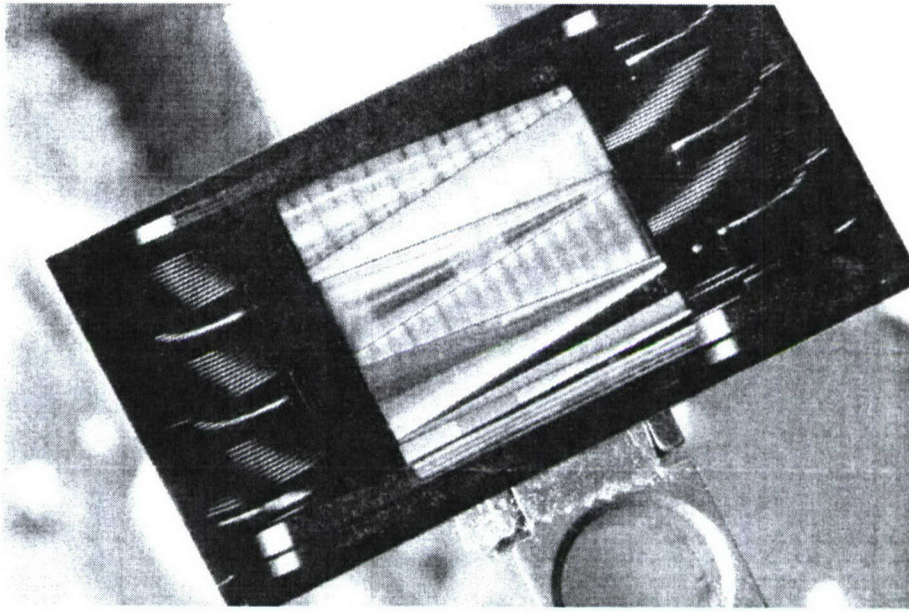


Figure 4. Family of test multiplexers based on HBRs in silica-on-silicon

### Phase and Amplitude Apodization for Advanced Filter Design

The passband of each channel is controlled by the relative amplitudes and phases of the diffractive contours that comprise each wavelength labeled section. LightSmyth has developed several important technical approaches for implementing continuous amplitude and phase variation between the diffractive contours that is fully functional even when employed with standard lithographic approaches. Standard approaches utilize a single diffractive contour etch depth across the entire fabrication wafer (as is lithographically convenient). Control over the amplitude and phase of each and every one of the family of diffractive contours provides very powerful and essentially arbitrary control over the spectral passband of each channel. Note that the passbands (central wavelength and profile) of all the multiplexer channels are independent. As a corollary of this fact, the device can support an essentially arbitrary combination of channel separations. Each wavelength-labeled section of the device in Figure 3 is essentially an integrated thin-film filter whose bandpass is lithographically defined.

As mentioned above, we have shown that lithographically scribed planar holographic devices have been shown to be spatially coherent up to centimeter scales. This means that spectral properties of HBR filters are limited only by fundamental spatial Fourier transform principles until very high spectral resolution (a few GHz) is required. In other words, the intrinsic bandpass of a simple HBR filter scales inversely with device length for lengths of a centimeter or less. For typical CWDM systems, including the 13-nm bandwidth commercial standard mentioned above, HBRs must either be very short (about 100 contours or 50-microns long) with quite high reflectivity per contour to achieve low insertion loss or possess some advanced apodization such as a spatial period chirp in order to provide a reflective bandpass of the required width. The use

of diffractive contours of high scattering strengths is undesirable for a number of reasons including typically high polarization sensitivity and propensity to exhibit high out-of-plane scattering loss. LightSmyth has explored the use of advanced spatial apodization together with more weakly reflecting diffractive contours to achieve HBR filters of required wide reflective bandwidths, low scattering loss, and low polarization sensitivity. With LightSmyth designs, HBRs with 13-nm reflective bandwidths tend to be 1-2 mm in length rather than the 50 microns that would characterize a Fourier-transform-limited device. More weakly scattering diffractive contours minimizes insertion loss and lengthening of the HBR is thus good.

### Achievable HBR reflective bandwidth

An important question bearing on the viability of HBRs as building blocks of coarse WDM multiplexers is the determination of the maximum reflective bandwidth that they can support. Reflective devices that rely on distributed diffractive contours always exhibit some frequency dependence. There is a coupling between the reflective strength of individual diffractive contours and the total reflective bandwidth that can be supported by an HBR device of a fixed size.

HBR devices are reflective in nature. More specifically, they depend on cooperative reflection from distributed arrays of diffractive elements (contours) each of which is by itself a weak scatterer. There are fundamental constraints that connect the total number,  $N$ , of diffractive elements in an HBR (or alternatively the length,  $L$ , of the HBR), the diffractive scattering

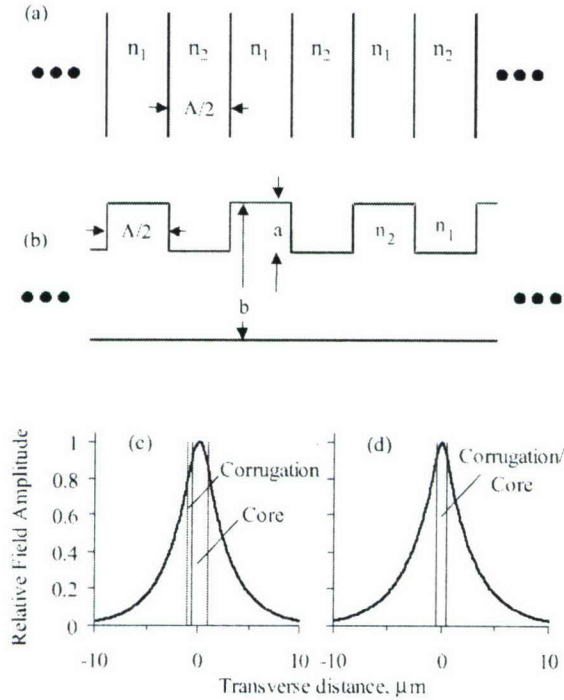


Figure 5. Schematic of distributed reflector stacks (a) and corrugated waveguides (b). Also shown are modal field distributions relative to the reflecting surfaces.

amplitude of each element,  $r_a$ , the total spectral bandwidth over which the device is to reflect,  $\Delta\nu_t$ , and the required reflective strength. Coarse WDM devices (e. g. a 16-channel multiplexer) require high reflectivity over an aggregate bandwidth that may be as large as several hundred nanometers. We wish to estimate the spectral bandwidth (which may or may not be contiguous) over which a first-order HBR of constrained length L and simple internal geometry can provide high reflectivity.

Consider the quarter-wave reflective stack shown in Figure 5a. The stack consists of planar interfaces between materials of refractive index  $n_1$  and  $n_2$ . Let  $\Delta n = |n_2 - n_1|$  and  $n = (n_1 + n_2)/2$ . The planar interfaces are spaced by  $\Lambda/2$  and produce strong Bragg backscattering at vacuum wavelength  $\lambda_B = 2n\Lambda$ . The incident wave (assumed incident normal to the interfaces) is attenuated and exhibits a 1/e penetration depth of approximately  $d = n\Lambda/q\Delta n$ . For the quarter-wave stack,  $q = 1$ . The corrugated slab waveguide of Figure 5b exhibits similar behavior except that the factor  $q$ , defined as the ratio of back scattered field amplitudes produced by the corrugation and plane interfaces, is less than one.

A regular diffractive structure of length  $d$  has a weak-signal Fourier-transform spectral bandpass of approximately  $\Delta\nu_d \approx c/4nd$ , where  $c$  is the vacuum light speed. We use this bandwidth to approximate that of diffractive structures of 1/e field penetration. In the following, we assume that an HBR of length  $L > d$  may be viewed as a number of segments of length,  $d$ , each of which has bandwidth  $\Delta\nu_d$  and operates at 1/e field transmission. To achieve a broad reflection band, the various HBR segments are chirped or frequency shifted. The construction described is consistent with an overall HBR reflection bandwidth  $\Delta\nu_{tot}$  given by

$$\Delta\nu_{tot} = \frac{L}{d} \Delta\nu_d = \frac{cL\Delta n^2 q^2}{4\Lambda^2 n^3}$$

### Reflective Bandwidth – Single Mode Architecture

We shift our attention to predicting how one produces an HBR capable of reflecting over several hundred nm with minimal insertion loss as needed for general CWDM mux products. In Figure 5d, we show the modal electric field for a 1- $\mu\text{m}$ -thick slab waveguide whose corrugations extend entirely through the slab ( $a=b$  in Figure 5b). The value of  $\Delta n$  is assumed to be 0.03. The  $q$  factor is found to be 0.16. With these parameters, we find that  $\Delta\nu_{tot} \approx 3 \times 10^{+13}$  Hz, which corresponds to about a 210-nm reflective bandwidth at the operative wavelength – broad enough to support 16 13-nm-wide CWDM channels. It should be noted the etch aspect ratio needed to produce the described broadband HBR device has been demonstrated as part of the LightSmyth development program. Note further that a wide range of HBR internal designs are possible providing even broader reflection bands and fully consistent with low loss at the fiber to die interface. It appears entirely possible to integrate much of the current functionality attributed to discrete thin-film filters into the fully integrated environment.

### Specifics of Multi-Mode Device Operation

The multimode HBR devices differ in important ways from the simpler single-mode devices.

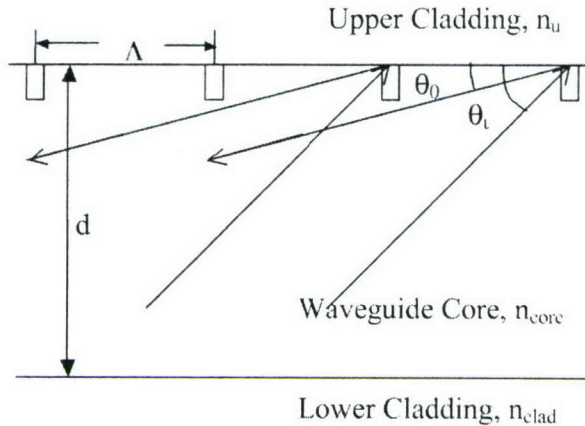


Figure 6. Geometry of back diffraction in a multimode waveguide

We give a brief overview of how the multimode devices work. In Figure 6 is shown the schematic geometry of light backscattering from diffractive elements within a multimode planar waveguide. The diffractive element geometry shown (located at the core/cladding interface) is simplified to facilitate definition of incidence angles for a representative input mode and a representative back-diffracted mode, but the following would apply to any diffractive element geometry. Each transverse optical mode within a multimode planar optical waveguide may be thought of as a superposition of two plane waves, each of which makes an angle  $\theta$  relative to the local plane of the waveguide (referred to as a propagation angle for the optical mode in question). Different transverse optical modes typically have different propagation angles  $\theta$ . The propagation angles  $\theta_{in}$  and  $\theta_{out}$  shown in Figure 6 represent, respectively, the angles made by the constituent plane wave subcomponents of input and back diffracted optical modes of the waveguide. Note that the input angle,  $\theta_{in}$ , and the back-diffracted output angle,  $\theta_{out}$ , are not shown as being equal. In general, the diffractive element set can back-diffract a specific input optical mode into the same counter-propagating optical mode or into one or more of the other counter-propagating optical modes of the planar waveguide. The relative strength of diffraction into the same or different transverse optical modes depends on the geometry of the diffractive elements and their placement relative to the core layer.

Each input-mode-to-output-mode diffraction process will occur most strongly at a unique vacuum wavelength. Diffraction will occur strongly at wavelengths satisfying the following equation:

$$\lambda/n_{core} = \Lambda(\cos\theta_{in} + \cos\theta_{out})/m \quad (1)$$

where  $m = 1, 2, 3, \dots$  is the diffractive order. The angles in Eq. 1 are, as described above, the characteristic modal propagation angles for the incident and diffracted optical modes, respectively.

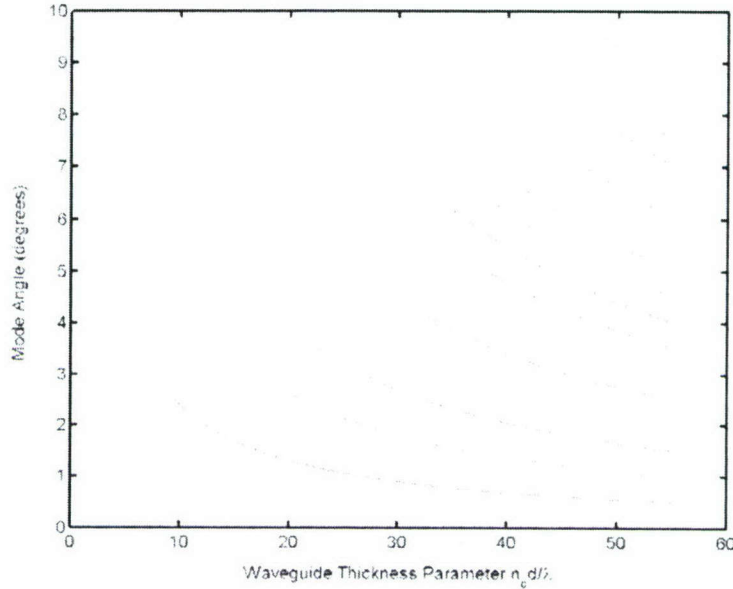


Figure 7. Propagation angles for modes in a multimode waveguide as a function of effective waveguide thickness.

In Figure 7, we plot the characteristic modal propagation angles for all modes that exist in a planar guide as a function of the effective guide thickness  $n_{\text{core}}d/\lambda$ , where  $d$  is the physical waveguide thickness. To calculate Figure 7, a core index  $n_{\text{core}} = 1.45$  and a cladding index  $n_{\text{clad}} = 1.43$  are assumed. As one moves to the right in Figure 7, the waveguide core is getting thicker. Additional optical modes are supported as the core thickness increases. As each successive optical mode “turns on”, its characteristic incidence angle begins near the critical angle of the core-cladding interface and then decreases as the waveguide becomes thicker. As the mode number increases, the modes become relatively evenly spaced throughout the angular range from  $0^\circ$  to the critical angle. Diffraction may occur from an input optical signal in any supported optical mode to a back-diffracted output optical field in any supported optical mode. If there are  $N$  supported modes, there are  $N^2$  potential scattering processes – some of which may be degenerate.

The maximum back-diffracted wavelength occurs for the lowest-order optical mode diffracted back into the lowest-order optical mode. The minimum back-diffracted wavelength occurs for the highest-order supported optical mode diffracted back into the highest-order supported optical mode. The interval between the maximum and minimum diffracted wavelengths,  $\Delta\lambda$ , can be approximated by

$$\Delta\lambda = 2\Lambda n_{\text{core}}(1-\cos\theta_H)/m \quad (2)$$

where we have approximated the propagation angle of the lowest-order optical mode to be  $0^\circ$  and the propagation angle of the highest-order supported optical mode to be  $\theta_H = \pi/2 - \sin^{-1}(n_{\text{clad}}/n_{\text{core}})$ . In many cases of interest, the diffracted bandpass width,  $\Delta\lambda$ , is quite small

relative to the diffracted vacuum wavelength  $\lambda$ . In such cases, we can approximate the diffracted vacuum wavelength as  $\lambda = 2n_{core}\Delta/m$  and calculate a fractional filter bandpass ratio

$$\Delta\lambda/\lambda = (n_{core} - n_{clad})/n_{core} \quad (3)$$

where we have inserted the definition of  $\theta_{II}$  into Eq. 2 to yield Eq. 3. The fractional bandpass for the portion of the optical signal diffracted by the diffractive element set of the multimode spectral filter is found to be simply related, via Eq. 3, to the refractive index difference between the core and cladding. A more accurate value of  $\Delta\lambda/\lambda$  for specific waveguide parameters can be calculated by standard methods, but for many design purposes, Eq. 3 suffices.

In Figure 8, the fractional bandpass of an exemplary multimode planar waveguide spectral filter with the core index 1.45 is shown as a function of cladding index. The fractional bandpass is approximately independent of the thickness of the waveguide core in the multiple transverse optical mode regime. It should be noted again that the waveguide need not necessarily have symmetric claddings. The fractional bandpass is essentially determined by the larger cladding index (i.e., the cladding index exhibiting the smaller index contrast with the core index). It may be desirable to have a relatively large refractive index differential when diffractive elements are formed from cladding material at a core-cladding interface, in order to increase diffraction strength or for other reasons. As long as one of the core-cladding interfaces has a sufficiently low refractive index contrast, the range of guided modes will remain small and Eq. 3 will typically suffice. An important design consideration for a multimode planar waveguide spectral filter is the degree to which the supported planar waveguide optical modes match the modes of input and output optical signal fields, for example optical modes supported by multimode optical

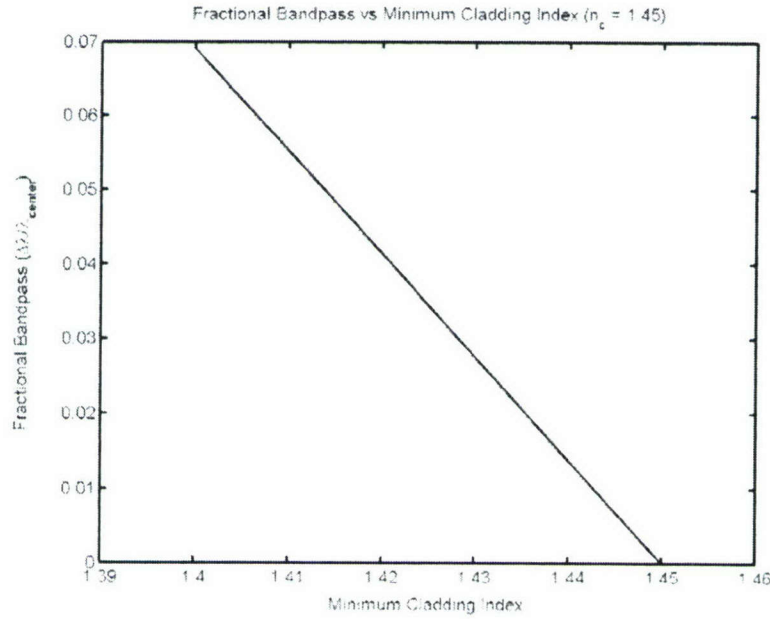


Figure 8. Fractional bandwidth arising from intermodal backscatter as a function of minimum cladding index

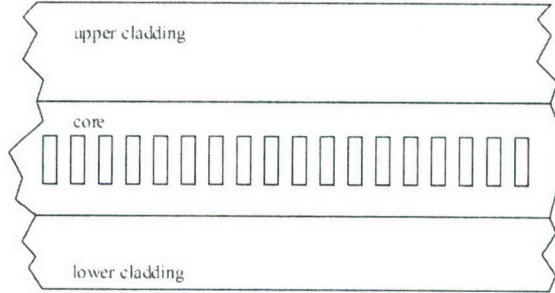


Figure 9. Waveguide with diffractive elements mostly spanning core

fiber. The value of  $n_{\text{clad}}$  not only affects the spectral filter bandwidth but also spatial mode matching to input/output optical signal fields. Minimal insertion losses will tend to occur when the respective angular spreads of the transverse modes supported by the planar optical waveguide and by input/output components (such as a multimode fiber, a multimode channel waveguide, an LED, a laser diode, and so forth) are substantially similar to one another.

### Reflective Bandwidth – Multi-Mode Architecture

In multimode waveguides, the situation is quite different from the single-mode case described earlier. The  $q$  factor described above is engineered to approach unity by extending the diffractive contours across most of the core waveguide channel (like Figure 9). This can only be conveniently done using UV exposure induced refractive index change within the multi-mode waveguide. (The distance is too long to etch.) The refractive index contrast available through direct refractive index change, however, is typically somewhat lower than in etched devices as UV-induced refractive index changes may be conservatively estimated to be 0.001. Plugging in the numbers, one finds that a multimode HBR can achieve reflective bandwidths of about 10-nm/cm. A family of multimode HBRs occupying a total length of 4 cm can thus collectively control about 40-nm total reflective bandwidth, which may be apportioned to discrete channels as desired. A 40-nm reflective bandwidth (at high reflectivity, i. e. 1-2 dB insertion loss) is sufficient for a custom coarse wdm mux/demux useful for upgrade of existing DoD systems. The available reflective bandwidth scales quadratically with achievable refractive index contrast. Some materials exhibit significantly higher UV-induced refractive index changes than the very conservative value mentioned above. Should we achieve an index contrast of 0.003, the available high reflectivity bandwidth of a 4-cm HBR product rockets up to 360 nm, which is more than adequate for even 16-channel coarse multiplexers with bandwidth specifications meeting the current commercial format.

### Overview of Phase II Objectives

- 1) Design single-mode coarse WDM multiplexer based on lithographically scribed planar holographic devices that meets current industry specifications for coarse WDM systems.
- 2) Design multi-mode custom coarse WDM multiplexer based on lithographically scribed

planar holographic devices modified to account for the multi-mode character of the guiding layer. Performance specifications to be comparable to single-mode device.

## Results of Phase II development

### Design Strategy for HBR waveguides

Figure 10 a-c shows cross-sections of different planar waveguide geometries and holographic structures. In Figure 10a, the planar hologram is realized as trenches that are etched into the waveguide core and subsequently filled with cladding material. In Figure 10(b) and 10(c) the planar hologram is fabricated in a unique grating layer that is part of a dual layer core architecture and located either adjacent to the lower (Figure 10b) or upper (Figure 10c) cladding.

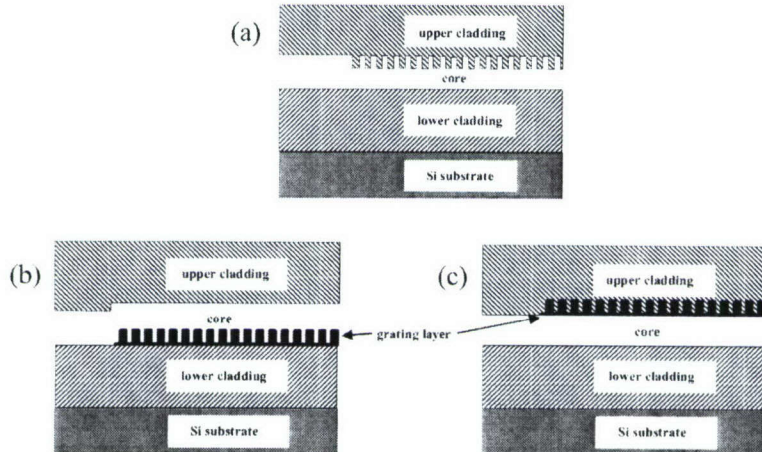


**Figure 10.** Planar waveguide cross-sectional geometries showing fiber attach and grating regions. a, single core architecture. The planar grating is realized at core-cladding interface. b and c, dual-layer core. The grating is realized in a separate grating layer adjacent to the bottom (top for c) cladding.

Two planar waveguide regions are critical for HBR multiplexer operation and require optimization. At the fiber-to-waveguide interface (to the left of the grating regions in Figure 10a-c) the waveguide has to be designed to yield minimal insertion loss when connecting to standard telecom single-mode fibers. Specifically, this requires matching of the planar waveguide eigenmode profile, a function of index contrast and waveguide dimensions, to the fiber mode. Second, the parameters of the grating region (containing the planar hologram) need to be chosen to yield high reflectivity over a spectral bandwidth sufficient to cover eight CWDM channels on a length scale consistent with the available device footprint. The band width over which high reflectivity can be achieved is a function of index contrast between core and grating layers as well as the overlap of the waveguide mode with the grating layer.

The results of our investigation are as follows: In the waveguide architecture shown in Figure 10a the core-cladding index contrast influences both the waveguide mode profile as well as the grating reflectivity. Consequently, the problems of fiber-to-waveguide coupling and grating

optimization become coupled and can not be addressed independently – a design difficulty. Furthermore, simulation results indicate that, for a given waveguide height, grating reflectivity does not scale linearly with index contrast but rather reaches an asymptotic value insufficient for operation over eight CWDM channels. This is due to the fact that mode confinement increases with index contrast effectively decreasing modal overlap with the grating.

The waveguide architectures shown in Figures 10(b) and 10(c) solve these problems by introducing an additional higher-index layer containing the planar grating. This uncouples the problems of low-insertion-loss fiber attach and high reflectivity grating region. The former can now be designed essentially independently by choosing an appropriate core-cladding index contrast and waveguide core height outside the grating region. Simulation results, backed up by prototype results, indicate that a 0.8 % core-cladding index contrast and a core height of 2  $\mu\text{m}$  will yield an optimized fiber-to-waveguide coupling loss of only 0.5 dB.

The properties of the grating region were found to be largely controlled by the thickness and index contrast of the grating layer. Optimized performance consistent with available fabrication technology was calculated to occur for a grating layer thickness of 1  $\mu\text{m}$ , grating etch depth of 850 nm, grating layer index of +2% with respect to the core layer and 1.6  $\mu\text{m}$  thick core layer. Our simulation results indicate that the architectures of Figures 1(b) and 1(c) should produce a reflective bandwidth of 400-500 nm at 1.5  $\mu\text{m}$  (with reflectivity > 85 %) fully sufficient to support eight CWDM channels.

### Initial multi-HBR device results

Two parameters are especially important in the design of HBRs. These are the reflective strength expressed as the  $e^{-1}$  penetration depth of resonant light into the HBR structure and the loss per unit length for non-resonant light propagating through the structure. To determine the value of these parameters and compare with theoretical expectations, the multi-HBR structure

shown in Figure 11 was designed and fabricated. The device comprises five separate 1-mm thick HBRs each having grating elements of circular structure. The HBRs are separated in wavelength so that, for example, if input light of  $\lambda_5$  is incident from the input port (at bottom) it passes through the first four HBRs, interacts with the last and is retro-reflected and focused to exit going out the input port. The device behaves similarly for the other wavelengths. (In HBR muxes, distinct output ports are employed.) It is found that losses are not evenly distributed about the HBR resonant frequency. When light passes through an HBR significantly above the resonant frequency, substantial losses accrue. Below and slightly above resonance the losses are very low when the HBR grating structure is first order. The asymmetric spectral distribution of loss generally requires that mux units be designed with HBRs arranged with resonances moving from blue to red as one moves deeper into the mux.

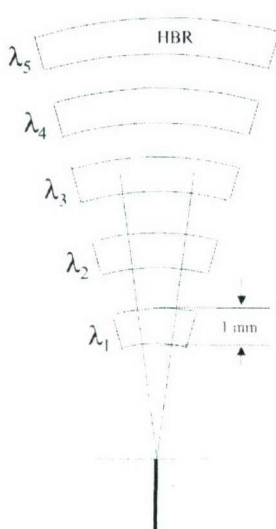


Figure 11

The structure of Figure 11 was fabricated in both single and dual core planar waveguides. The dual core device is expected to produce much

stronger HBR reflectivity. The reflection spectrum of the Figure 11 device fabricated in a single core wafer with 450-nm-deep etched diffractive contours and a 2-micron-thick core is shown in Figure 12. In this case, the  $e^{-1}$  extinction length is longer than each 1-mm HBR, i.e. the devices are in the weak reflection limit, and the spectral reflection passband is approximately proportional to the Fourier transform of the HBR internal structure (which in the present instant is a simple first order grating without apodization). The insertion loss is 6-7 dB with much of this loss associated with the low reflectivity of the HBRs. Note the uniformity in strength of the reflections indicating excellent low-loss focusing from HBRs of various radii, which implies very high optical homogeneity within the relevant optical propagation paths and low scattering/absorption/etc losses.

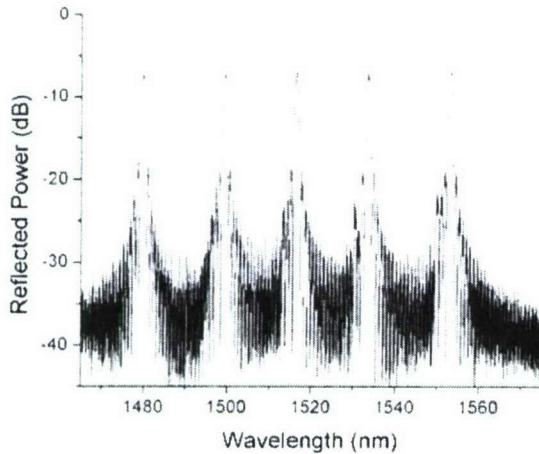


Figure 12

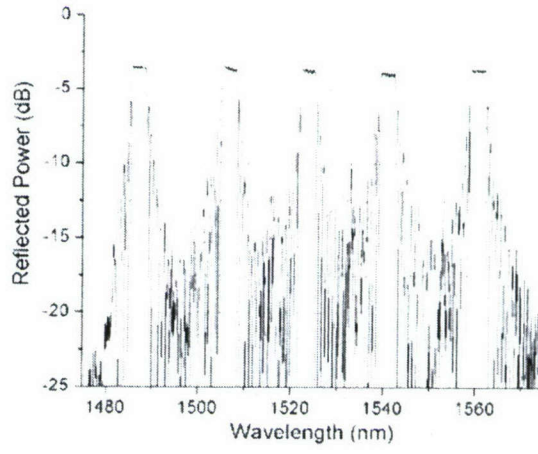


Figure 13

In Figure 13, we show the reflection spectrum of the same 5-HBR structure when implemented in a dual-core planar waveguide. The core consists of a 2-micron-thick layer and a one-micron-thick layer whose index is 0.03 higher. (The index difference between cladding and low index core is 0.01 and all materials are silicon dioxide with various dopants with absolute indices in the range 1.44 - 1.49.) The HBR diffractive contours are etched in the higher index core layer and filled with the lower index core layer. The reflectivity of the dual-core device is dramatically higher than the single-core device. The total insertion loss is now somewhat over 3 dB which represents the coupling loss at the fiber to planar waveguide interface (two transitions). Normally this coupling loss is less than 1 dB, but the current device was not optimized for coupling. The insertion loss associated with the HBR reflectivity is essentially zero. The broadening of the spectral passbands arises from the extreme strength of the HBR reflectivity. The  $e^{-1}$  extinction length for resonant light interacting with the HBR is deduced to be approximately 270 microns. The effective length of the HBR becomes approximately equal to the extinction length and thus the passband is broadened (via standard variation of passband with inverse of the effective length).

The results of Figure 13 are very important. They confirm that the HBR device implemented in low index contrast silica waveguides can produce passbands wide enough to meet the requirements of CWDM multiplexers. In fact, the coupling we have achieved via our unique

dual-core design is somewhat of a world record (in silica). Based on the current extinction length, we calculate that a 1-mm HBR can support a high reflectivity passband width up to approximately 15 nm (in the 1.5 micron spectral regime). Current DUV photolithography tools available to us allow for the fabrication of devices up to 3 cm long. Based on these results, we can conclude that the 8 HBRs for an 8-channel CWDM mux will require as little as 8 mm total length, providing a large safety margin for adequate design. Actual CWDM HBR mux units will be somewhat longer than 8 mm, because apodization will be employed to provide a more rapid passband falloff than is obtained with a step-function-type HBR grating.

Another important aspect of the results shown in Figure 3 is the absence of increased insertion loss as one moves from the leftmost HBR passband to the rightmost. The rightmost passband involves optical signals that have traveled through the first four HBRs (non-resonantly) without incurring loss. It has been common belief in the integrated optics community that HBR-like grating structures are lossy. We demonstrate here conclusively that properly designed HBR units are very low loss. Our measurements of Figure 3 are consistent with zero non-resonant loss. Of course, loss must occur at some level, but it is too small to clearly appear in the measurements.

It should also be noted that the observed HBR reflectivities are consistent with coupled mode calculations. This result is not always obtained. In some previous fabrication efforts, reflectivity observed was low compared to theory. This appears to arise from dopant diffusion and deformation of grating structures when device anneal temperatures are too high. We devised a custom fabrication process that preserves design structure through the various annealing stages by careful temperature and anneal time control. This custom fabrication process is an important advance and is not the standard process used in the integrated photonics industry.

### **First Realization of Low-Loss, Flat Passband Filtering Function**

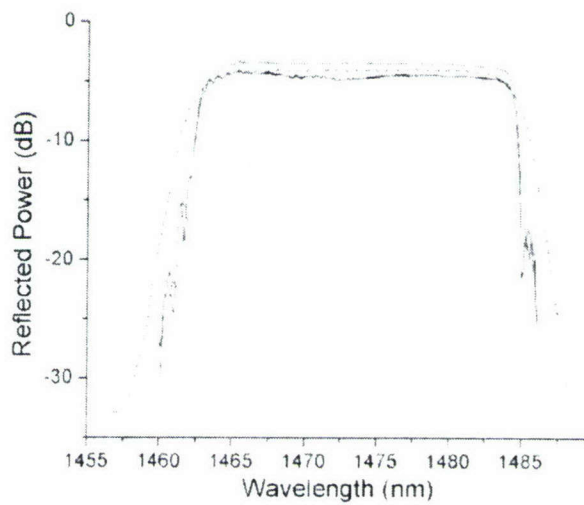


Figure 14. First successful flat passband, low-loss, HBR filtering function

Coarse WDM filters are special in that they must support broad (13-16 nm) very flat-top passbands. They must also be compatible with coupling into single-mode fibers. Of all existing filtering technologies, only thin-film filters and a special dual arrayed-waveguide grating (AWG) structure have been shown compatible with all of the requirements. The latter dual AWG approach has not yet demonstrated generally acceptable insertion loss levels and occupies a large footprint. Other technologies including reflective surface gratings (integrated or free-space) and arrayed waveguide gratings have difficulty in producing broad passbands with acceptable loss when single-mode outputs are required. Fiber gratings can produce the desired passband shapes and are compatible with single mode output, but the index contrast that can be created via UV photoexposure is too small to produce high reflection strength over the required passband in a convenient fiber length.

Thin-film filters thus currently provide the approach of choice for powering CWDM multiplexers. Mux devices based on thin-film filters are not compatible with integration and comprise assemblies of many parts and require multiple precision optical alignments. It is thus a major milestone to demonstrate an alternative integrable technology that is capable of providing broad bandwidth, flat-top, single-mode filtering solutions and is further compatible with low-cost stamping-based replication. Such flexible filtering solutions will likely provide the core building block elements to build tomorrow's optical transport links within chips, between chips and boards, and between computers in local high bandwidth networks as would be found in aircraft, ships, as well as civilian environments.

In Figure 14, we show the first successful HBR filtering function exhibiting all functionality needed to implement fully integrated, broad and flat passband, multiplexing units.

A single Holographic Bragg Reflector (HBR) of 4.8 mm length in silica-on-silicon dual-core waveguide format was designed and fabricated. The HBR comprised approximately 10,000 discrete etched circular contours that image between the input port and output ports. To achieve the wide design passband, the spacing between the HBR contours was spatially chirped with the shortest spacing on the input end. The HBR was also apodized using the correlated line set method invented by LightSmyth (Optics Express **13**, 2419 - 2416 (2005)).

The measured reflective passband of the prototype HBR is shown in Figure 14. The two solid traces represent orthogonal input polarizations. Importantly, separate measurements reveal that the difference between insertion loss of the two polarizations stems in large part from coupling into the channel waveguides used to access the HBR. Channel waveguides employed in this first prototype are not optimized and industry solutions are available to provide low polarization dependent coupling. The -1 dB bandwidth of the filter is approximately 20 nm – more than enough for a single CWDM channel. The filter is operating in saturation. The upper solid trace exhibits substantially less than 1 dB variation in reflectivity across the passband. The lower solid trace, exhibits a small dip near the center of the passband. Additional measurements suggest that this dip results from wavelength-dependent coupling into the channel waveguides for the relevant polarization along with a small polarization-dependent bending loss in the access channel waveguides. These channel waveguide effects can be eliminated by methods well-known in integrated optics. The dashed line is a theoretical evaluation of the filter performance

value in the low reflectivity limit, which is not strictly satisfied in the present device. Nevertheless, the model reasonably predicts the width and flatness.

From the performance depicted in Figure 14 (a first prototype device), we can conclude that HBR devices hold great promise as a building block of integrated broad band and flat top filters. As development proceeds, refinement of channel waveguide coupling (not fundamental to HBR performance) will be an important objective. Most insertion loss and polarization effects observed in Figure 14 can be traced to unoptimized performance of the channel waveguides used in the first prototype.

### Preliminary 4-channel CWDM multiplexer/demultiplexer

Preliminary 4-channel mux devices are tested and performance analyzed. Spectral channels corresponding to HBR devices located deeper into the chip are seen to exhibit undesirable losses for TE polarization. Design factors associated with observed losses are identified and pathways to eliminating loss in subsequent mux test devices described.

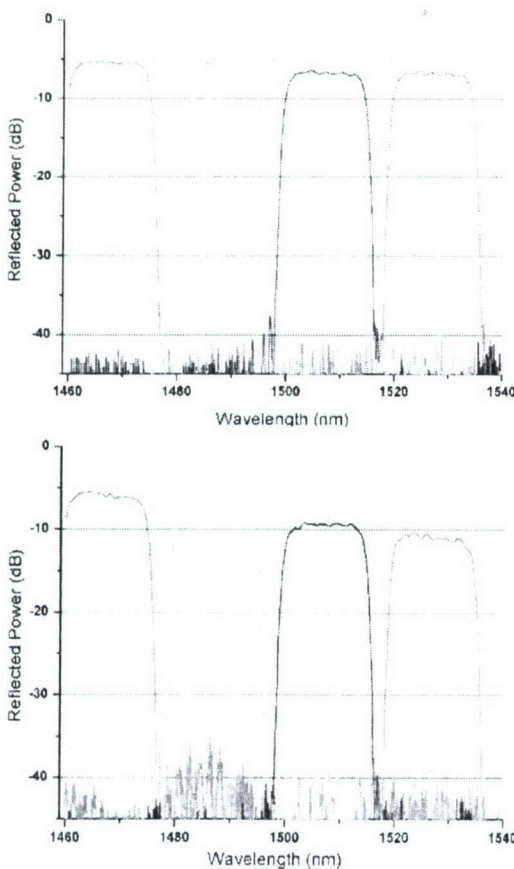


Figure 15: Reflected power from four channels of a first prototype 3-line apodized CWDM mux. Top (Bottom) TM (TE) polarization

In Figure 15, we show the reflected power passbands of four channels from a first-round CWDM mux prototype. All HBR-based filters must be apodized so as to produce spectral transfer functions that fall off quickly and do not interfere with adjacent channels. In the mux of Figure 15, the apodization was achieved using the 3-line correlated line set approach ([Interferometric Amplitude Apodization of Integrated Gratings](#), T. W. Mossberg, C. Greiner, and D. Iazikov, Optics Express **13**, 2419 (2005)). The internal grating configuration used in correlated-line apodization is shown in Figure 16.

The four HBR gratings associated with the

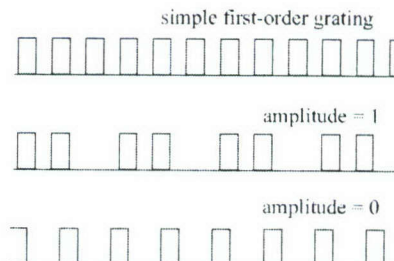


Figure 16: Top: simple first-order grating; Middle: correlated-line apodization maximum reflectivity; Bottom: correlated-line apodization zero reflectivity

respective mux channels are positioned sequentially so as to increase the distance from the mux chip input. The shortest wavelength channel is positioned closest to the input port and adjacent output port array. The sequential arrangement means that signal in the longest wavelength channel must travel through the first three HBR structures twice, first on entry and again as it exits to the output port. Losses accrued by the longer wavelength channels on passing through prior HBR gratings must be eliminated.

In the present fabrication run, we see that the total insertion loss of the first channel is about 5 dB. Of this loss, approximately, 2.5 dB is determined by auxiliary measurements to correspond to fiber-to-chip coupling (which is not optimized and has been demonstrated in other examples to be less than 1 dB). Approximately 2 dB of the remaining channel 1 loss comes from low grating reflectivity. The HBRs in this fab run were designed prior to firm calibration of reflectivity vs device length. The HBRs were designed to be too short and thus exhibit lower than optimal reflectivity. HBRs of longer length were tested also (as part of separate test structures) and found to have insertion loss figures limited only by the fiber-to-chip coupling loss. Thus about 4 out the 5 dB insertion loss of channel 1 will be eliminated by simple design changes (better fiber-to-chip mode matching and a longer HBR grating – the present HBRs are only 1.9 mm in length). The third and forth channels in the top of Figure 15, exhibit an increased insertion loss. Measurements indicate that this additional loss comes from bending losses in the channel waveguides used to access these two channels. These structures were designed prior to complete characterization of the fab process and the bending losses are easily avoidable by small index, waveguide profile, and bending radius tweaks. We note that passbands and adjacent channel isolation is excellent.

In the bottom portion of Figure 15, we present the behavior of the same mux device with TE polarization (the top section is TM polarization). In the case of TE polarization, a loss increase with increasing channel wavelength is seen. We have analyzed this result and find that it is caused by the specific HBR apodization method employed in this device (see Figure 16). In this early design run, we used simple deleted line correlated-line-set apodization. The middle and bottom sections of Figure 16 show the grating structure at full and zero reflection amplitude, respectively. It will be immediately noticed that the apodized gratings have spatial Fourier components with periods longer than the primary spacing (top grating). Existence of these longer period Fourier components engenders polarization-dependent out-of-plane scattering for TE polarization (the radiation pattern of TM polarization discriminates against the dominant out-of-plane scattering directions). It is this out-of-plane scattering that produces the increased loss with increased length of propagation through the HBR structures.

We have several solutions available to this problem. First, lines are deleted in the correlated line apodization approach in order to prevent lithography error as grating lines move in position and get close to one another. In the device under consideration here, every third line was deleted regardless of need. In later designs, lines were deleted from the simple first order grating configuration only when calculation indicates lithographic resolution problem. A substantial decrease in the amplitude of longer period grating Fourier components was achieved. Additionally, the correlated-line-apodization approach works with line sets of arbitrary number. We are designed the apodization profiles with line-sets of 9, 13, 17 and other line numbers. Increase in the correlated line set size provides another means of decreasing the net amplitude of

long-period spatial Fourier components in the HBR gratings and thus decreasing TE polarization loss. Also design options involving entirely different approaches to amplitude apodization, to be described in the next section and further below, were latter utilized. The basic requirement in reducing TE polarization loss on propagation through non-resonant HBR structures is to eliminate long-period spatial Fourier components from the HBRs.

### “Accordion” Apodization

We examine various apodization approaches that minimize out of plane losses for the TE polarization.

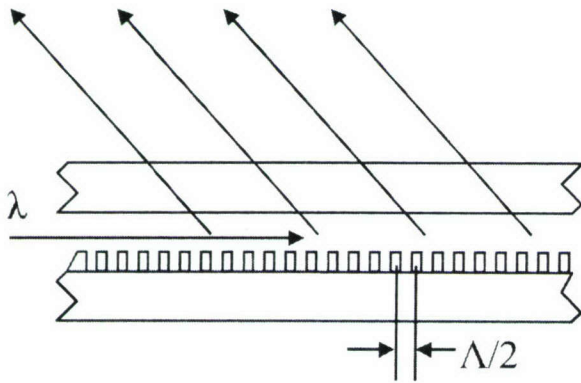


Figure 17. Uniformly spaced waveguide diffractive structure showing out-of-plane scattering

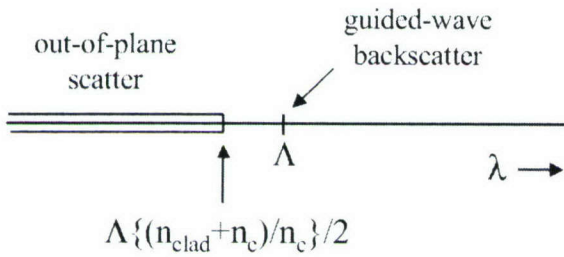


Figure 18. Wavelength line showing which wavelengths scatter and to where in a uniform waveguide diffractive structure of spacing  $\Lambda/2$ .

scattering prior to interacting with their resonant diffractive structure. The gap between resonant backscattering and the out-of-plane loss scattering can be traced to the difference in magnitudes of the guided and cladding mode wave vectors and can be useful in limiting loss.

When a diffractive structure is apodized, the well-defined spatial period of the structure is

In Figure 17, we depict a planar waveguide with a uniform, etched, distributed diffractive structure. Light of in-medium wavelength  $\lambda$  incident through the guiding layer from the left may coherently diffract from the diffractive structure. When  $\lambda \approx \Lambda$ , the light will backscatter in the guiding layer, back along the direction it entered. In Figure 18, we plot wavelengths that can scatter from the waveguide grating of Figure 17. The backscatter resonance is shown. Also shown is a continuous band of waveguide-incident wavelengths that scatter out of the plane. Here  $n_{\text{clad}}$  and  $n_c$ , respectively, represent the cladding and core effective refractive indices. Scattering out of the plane may be useful in some cases, but in the present CWDM application where all waves should remain guided, the out-of-plane scattering represents loss. The absence of out-of-plane scattering for wavelengths longer than the backscatter resonance wavelength, allows diffractive structures for various multiplexer input wavelengths to be stacked with the shortest wavelength reflector first so that signals do not pass through diffractive structures capable of producing out-of-plane

broadened into a band of spatial Fourier components each of which can generate an out-of-plane loss band like that shown in Figure 18. When the apodization produces grating spatial frequencies whose wavelengths are red shifted relative to desired signal wavelengths by more than the scattering gap (see Figure 18), those spatial frequencies contribute loss.

The trick in producing an apodization scheme with low loss is found to involve creating a spatial structure whose spatial frequencies are primarily higher than the unapodized uniform spatial frequency yet correctly apodizes the structure for interaction with the optical signal. In our early apodization approaches, the spatial Fourier spectrum produced tended to be symmetrical about the original spatial frequency and was thus capable of generating scattering from the long wavelength spatial components. We have also developed and implemented an approach that tends to produce primarily shorter wavelength spatial Fourier components and should reduce out-of-plane loss.

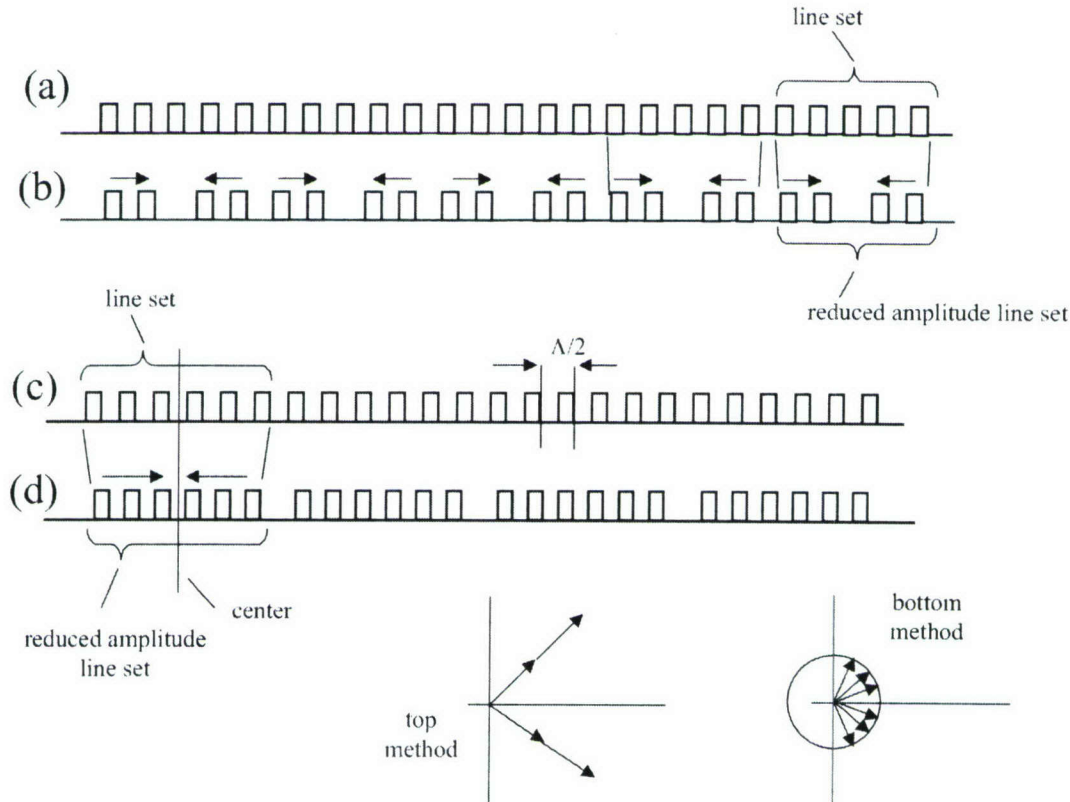


Figure 19. Two correlated line set approaches to amplitude apodization. In top (a,b), spacing between line pairs is constant. In bottom (c,d), spacing between all lines in the correlated set decreases. Second method produces blue biased spatial Fourier spectrum = good. Phasor representations of net reflected amplitude in both cases are shown at bottom.

In Figure 19, (a) and (c) represent uniform diffractive structures. (b) represents our earlier correlated line set approach to amplitude control. In (b), a set of five lines is reduced to four, the outer pairs are center shifted while maintaining the intra-pair spacing. The net reflection amplitude of the correlated line set may be continuously controlled by varying the spatial shift of the outer pairs. The apodized structure's spatial Fourier spectrum is largely symmetric about its original well-defined unapodized spatial frequency and the long-period Fourier components can

contribute to loss.

In Figure 19 (d), another approach to continuous line-set amplitude control is shown. In this case, sets of lines are given shorter periods. The shortness of the period controls the net reflectivity at the operational signal wavelength. Because the line spacing typically becomes smaller, the overall spatial Fourier spectrum of the structure is biased blue. Few red-shifted spatial Fourier components are generated and the resulting out-of-plane scattering loss at the operational signal frequency is simulated to be substantially reduced. We call this approach to apodization the “accordion” apodization approach.

### HBR Fabrication Process

To fabricate HBR devices incorporating the ideas described in the last several reports, an extensive series of steps is followed. These steps are described in this section.

The first step in the fabrication process is the allocation of space within the 25x33 mm DUV photolithographic stepper field. Each HBR-based multiplexer typically requires a rectangular space of 4 mm x 25 mm. Owing the high costs of fabrication and mask making – many of which do not scale with the number of designs within the available stepper exposure field, the field is densely packed with different devices, some multiplexers, some general test structures. In a typical fabrication cycle, six entirely separate CWDM multiplexers using different apodization approaches were selected. Additionally, fifty or so channel waveguide grating structures are included to test 1D copies of the 2D HBR grating patterns.

The second step of designing the apodized HBR’s comprises several sub-steps. First, software is written to calculate the amplitude and phase apodization that is required to give the passband profile desired. The output of this step is a function of amplitude and phase from front to back of the HBR controlling one channel of a multiplexer (for example). The apodization functions obtained are simply mathematics and need to be translated into physical device characteristics by an apodization approach consistent with device fabrication using purely binary etch – for cost effective implementation. Separate software programs are written for each method of apodization and the mathematical apodization is translated into the precise position of thousands of individual contours that actually comprise the HBR. Next, additional software is written to convert the line spacing information into a set of points that mathematically represents each and every contour. This set of points (the HBR point image) is fed into yet more LightSmyth written software that simulates, via numerical diffractive scattering calculations, the actual behavior expected from fabricated devices. The HBR point image typically comprises millions of points. Calculations of simulated performance are lengthy.

Once a convergence of desired passband and simulated passband emerges, the HBR point image data is input to commercial electronic mask layout software. The complex diffractive HBR structures are written segment by segment. Up to a million or so straight line segments are used to represent the focusing contours of an HBR. Of course, care is taken to ensure that the error between straight-line approximations to curved contours is consistently less than a tenth wavelength (depending on specific design). The mask layout software is used to generate a GDS2-format mask image, which is sent to a mask vendor for fabrication.

In addition to the diffractive-level mask, a waveguide-level mask is required to provide optical access from the edge of each die to the slab waveguide region wherein the HBR's are situated. The waveguide-level mask is laid out with the same commercial mask layout software.

Once the two masks have been produced, the two-layer fabrication process can be set in motion.

### **Product Level HBR multiplexer Performance**

Incorporating the design ideas and improvements described above, we produced a series of wafers whose HBR multiplexers displayed product level performance.

A number of wafers were produced with single-core and dual-core construction. In the case of dual-core wafers, three different thickness of the grating material layer were employed. The different grating material thicknesses (and corresponding different grating etch depths) result in quite different grating-field coupling strengths. Also, the thickness of the grating material layer is found to significantly influence the polarization dependent wavelength shift of the devices. Several multiplexers were designed and fabricated. We first describe an unapodized 8-channel multiplexer.

#### Eight-Channel Multiplexer

In Figure 20 is presented the transmission spectrum of 8 separate channels of an HBR-based CWDM multiplexer. The die has one input channel waveguide and eight output channel waveguides. Eight separately oriented and spatially successive HBRs control the coupling between the input and the various outputs. Figure 1 shows the superimposed output reflection

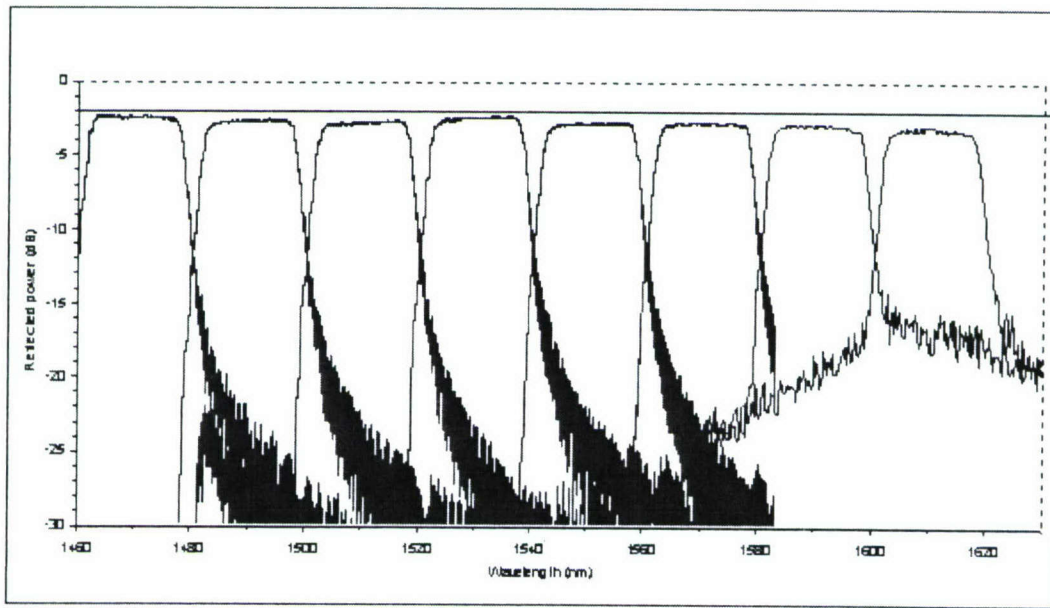


Figure 20. Eight-channel unapodized CWDM multiplexer

spectra of the eight output channels. The data at right was obtained via a filtered white light source as available lasers did not operate at the appropriate wavelengths. The noise floor of the filtered white light source was substantially higher than the laser source. Each HBR in this multiplexer had a chirp in diffractive line spacing so that its reflection bandwidth could be expanded to fill the design CWDM bandwidth. There was no apodization to suppress passband wings. This unapodized device was fabricated so that we could ultimately compare its behavior with more advanced apodized devices exhibiting much more rapid wing falloff. Also, a simple chirp design introduces the smallest possible range of spatial frequencies into the grating structure. As pointed out in previous sections, the introduction of a wide range of grating spatial frequencies can lead to unacceptable loss.

Important points to note: The device is the world's first fully integrated flat-passband CWDM multiplexer that is capable of functioning in a fully single-mode environment, i. e. both input and output may be single-mode ports. The maximum insertion loss (fiber-to-fiber) is about 3.5 dB while the bluest channels have only about 2 dB of insertion loss. Of this loss, approximately 1.5 dB comes exclusively from fiber-to-die coupling. As this is a first prototype, both fiber-to-die coupling and HBR insertion loss can be expected to be significantly improved in follow-on development. The wing falloff agrees with simulation for an unapodized linear chirp (in the high reflectivity limit) and will be substantially improved in apodized devices. The polarization dependent loss and wavelength shift are negligible. The device is athermal over an operating range of about 120 C. Only high-part-count, free-space, thin-film-filter-based devices could previously provide the single-mode performance shown in Figure 20. The multiplexer die size is approximately 4 mm by 20 mm. Cost and performance advantage relative to previous technologies is profound. The small die requires only a simple package without temperature stabilization and likely without hermetic sealing. But final packaging constraints will be revisited at a later time.

It should be noted that the aggregate reflection bandwidth achieved in the eight channels is more than 120 nm. To provide nearly total reflection over such a large bandwidth with less than 20 mm of waveguide grating is a very powerful result. UV-written Bragg gratings generally do not have intrinsic reflectivity large enough to produce wide bandwidth total reflectors with reasonable lengths – long filters can introduce undesirable group delay ripple. LightSmyth has put man-years into the development of strong and low loss gratings. The results obtained are a pleasant confirmation that the original projections concerning achievable reflectivity and bandwidth were correct. Holographic Bragg reflectors function analogously to thin-film filters and may be considered integrated thin-film filter equivalents.

In high index guiding layers like silicon, integrated HBR devices should provide even stronger grating-field coupling. HBR devices and multiplexers may be essentially useful in silicon photonics as their low loss character will be an improvement over alternatives.

#### Four-channel apodized, high performance, integrated HBR mux

The eight-channel mux described above is unapodized, which means that the wings of its spectral passbands are relatively slowly falling – in accordance with basic Fourier principle. To produce spectral passbands with rapid fall-off, it is necessary to introduce amplitude and phase

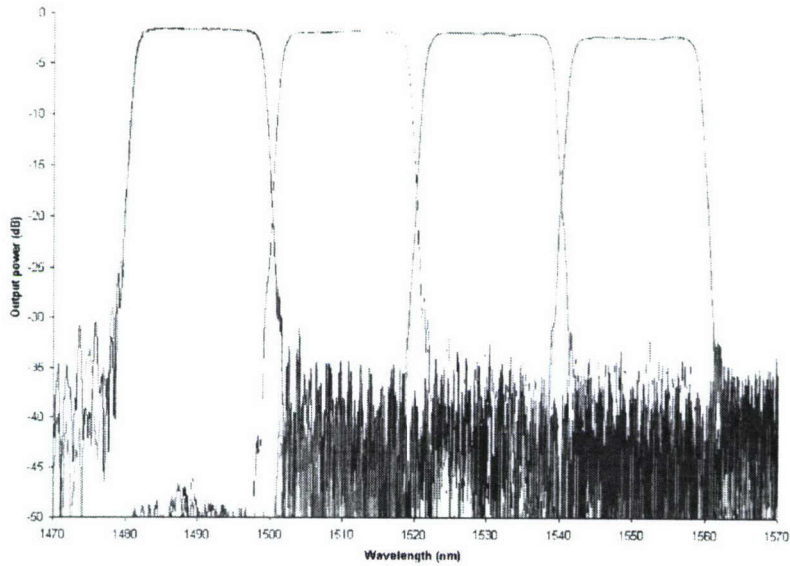


Figure 21. High performance, integrated, apodized, HBR CWDM multiplexer/demultiplexer

variation into the reflectivity as a function of position of the HBR mirrors. In Figure 21, we present measurements of a four-channel multiplexer whose HBR's were amplitude modulated using the “accordion” method (see above).

It will be recalled from the discussions of previous reports that the challenge of introducing position-dependent reflective amplitude in HBRs follows from the binary nature of standard semi-conductor etch methods. Our HBR devices comprise curvilinear trenches etched into a slab waveguide core-cladding interface. Simple etch methods provide trenches of essentially the same depth and hence reflectivity. Apodization requires variable reflectivity which could simply come from variable etch depth, but such depth variation is inconsistent with standard fabrication. Our approach to introducing amplitude control while using binary etch is to use interference in the reflections from groups of trenches to control the overall reflectivity of the trench group even though all the individual trenches have uniform depth and reflectivity. In the accordion method, groups of trenches are displaced toward a common center with the spacing between all trenches in the group remaining uniform. The resultant diffractive region, considered as a short grating segment, becomes blue-shifted relative to its nominal operating wavelength and thus has lower reflectivity, since it is detuned.

We designed and fabricated a four channel mux apodized with the accordion method with channel HBRs comprised of trenches whose spacings also exhibit a slow spacing chirp in order to create a large reflection bandwidth. The accordion apodization is employed at the edges of the HBR to reduce reflectivity relatively slowly rather than abruptly at the end of the trench array. The accordion apodized device performance is shown in Figure 21.

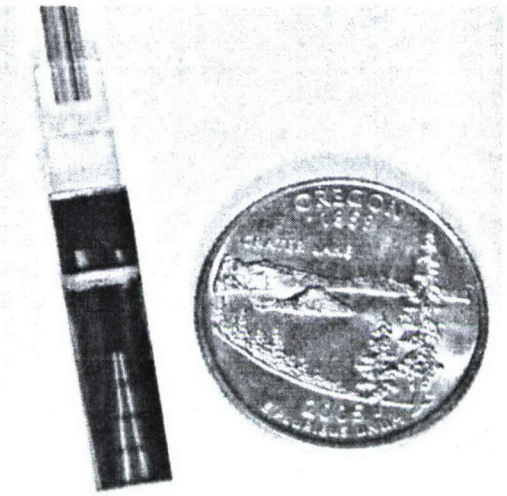


Figure 22. Photograph of 4-channel mux of Figure 21 connected to fiber array I/O

The channel passbands are uniquely flat, unprecedented performance for an integrated device with such low insertion loss. It will be noted that the passband wings fall off quickly at a rate of roughly 10-12 dB/nm. The TE and TM polarization results are both shown overlapped in Figure 21. It can be seen that the polarization-dependent loss is only about 0.2 dB. Also, the polarization dependent wavelength shift is negligible. The polarization-dependent wavelength shift is controlled by the dual layer core geometry devised by LightSmyth to balance various structural and strain factors to achieve very low birefringence. The device is passively athermal.

The device performance shown is product level and clearly disruptive. The designs demonstrated here are the only ones ever constructed in an integrated environment that can produce a competitive integrated CWDM mux for single-mode systems. Variants can be expected to work in stamped/injection molded polymer format and in the silicon photonic format.

In Figure 22, we show a 4-channel CWDM accordion mux chip with a v-groove fiber array attached. The device size is small to a record breaking level. A prototype of this device, like that shown in Figure 22, was shipped to various potential customers including Lockheed-Martin who verified our test results.

Only one wafer with the accordion mux design has been produced so issues about yield are not yet clear or optimized. It was noted that in some of the chips from this single wafer, insertion loss increased strongly for signals as a function of physical depth into the device. We tentatively attribute this to inhomogeneities in the various film layers comprising the planar waveguide that occurred for certain regions on the wafer. Such inhomogeneities will lead to a defocusing and

shifting of the optical signal beams that accrues with propagation length, i. e. depth into the device. It is believed that attention to this issue in subsequent fabrication runs will eliminate or at least substantially reduce this issue.

### **Split-Contour Apodization**

We now describe measurements and principles behind an alternative approach to HBR apodization, i.e. wavefront splitting apodization. Unlike methods described above, this apodization approach makes explicit use of the 2D nature of HBRs. In this method, portions of the signal spatial wavefront are differentially phase shifted, which through interference at the output port leads to output amplitude (and phase) control. We describe the method, measurements of a test implementation, and describe aspects of the device performance that are not yet understood.

It is crucial in the implementation of planar waveguide spectral filters to provide for flexible passband control, which does not introduce unacceptable loss. As described above the introduction of diverse spatial Fourier components into the structure of a distributed diffractive structure can lead to loss. Structure Fourier components with k-vector magnitude less than the operative signal k-vector magnitude because they can produce out of plane scattering and hence loss. It is good to avoid apodization methods that create red-shifted structure Fourier components. The ultimate low-loss integrated diffractive structures will have no spatial Fourier components red-shifted relative to the signal.

The correlated line set apodization approach (of which the accordion method, described previously, is a variant) allows for reflective amplitude control by the relative displacement of individual diffractive elements (grooves or trenches) within a small set of such elements so as to interferometrically control the overall reflective amplitude of the set to desired values even though each diffractive element (constructed with binary etch) always remains at constant reflectivity. The displacement of individual diffractive elements away from simple periodic spacing, introduces additional spatial Fourier components into the structure. The accordion method of interferometric amplitude control is essentially a near single-sideband spatial modulation approach. The displacements of diffractive elements in accordion apodization are chosen so that the blue shifted spatial Fourier components are heavily favored relative to the lossy red-shifted spatial Fourier components. However, the red-shifted spatial Fourier components are not completely zeroed in accordion apodization and losses are not completely suppressed, although as the 4-channel apodized mux results clearly demonstrate, residual losses can be so small that they do not interfere with meeting specs for CWDM multiplexers. Nevertheless, it is useful to explore whether alternative apodization approaches exist that allow for even more perfect elimination of lossy, red-shifted, apodization-introduced, structural Fourier components.

The whole family of correlated-line-set apodization methods is a one-dimensional solution that could be implemented in channel waveguide gratings, fiber gratings, or thin film interference filters. The HBR devices are two dimensional. Are there uniquely two-dimensional approaches to apodization control that provide optimal suppression of undesired spatial Fourier components in the diffractive structures? We believe that there are. Instead of moving individual diffractive

elements in one-dimension to interfere with one another, in a two-dimensional device one can split a single diffractive element (i.e. grating line analog) into two or more pieces. Each piece still provides focusing from input to output port, but by splitting the single diffractive element into multiple pieces and spatially shifting the diverse pieces (therefore phase shifting the out-coupled signal from corresponding pieces), one can interferometrically set the net output field reflected from the diffraction element to any value desired.

In the HBR, stacks of diffractive elements across the signal wavefront are differentially displaced. Within a single stack, the diffractive elements have nearly perfect periodicity except for an overall slowly varying spatial phase shift relative to other diffractive element stacks introduced to produce the desired spatially varying amplitude apodization. The displacements of diffractive elements within a small set such as that which occurs in correlated-line-set apodization methods (one-dimensional) introduces high spatial frequency Fourier sidebands including lossy red-shifted sidebands.

In Figure 23, we graphically portray diffractive element contours as used in wavefront splitting apodization. In part (a), all rays emanating from the input port reach the output port in phase. In part (b), half of the diffractive element is displaced from its original position. Consequently, rays striking the two diffractive element regions travel different path lengths and arrive at the output port with a phase difference directly proportional to the displacement between diffractive element sections. By varying the displacement, one controls the net reflection amplitude. In the HBR, hundreds or thousands of diffractive elements are present. These elements are divided into stacks with a stack comprising, for example, one side of the split diffractive element of Figure 23b.

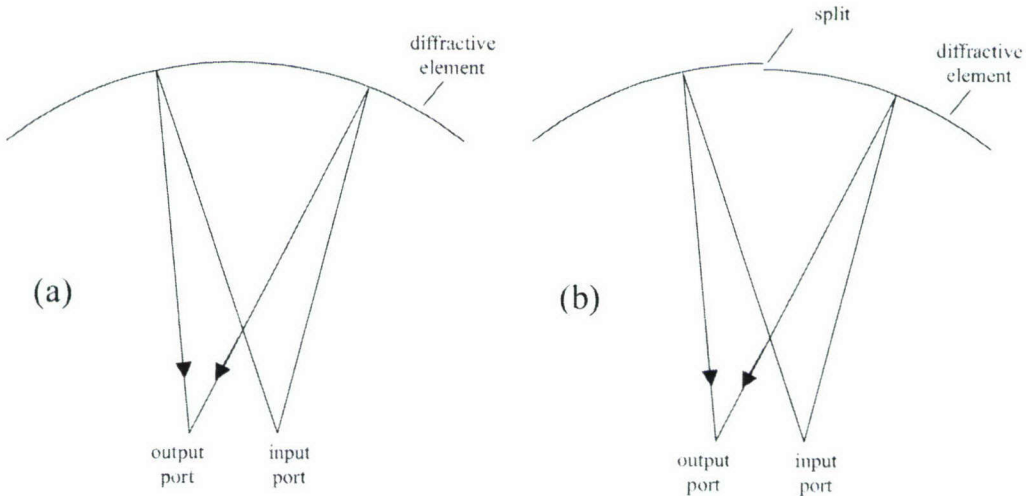


Figure 23. (a) Continuous HBR contour; (b) split HBR contour with controlled displacement for control of net reflected amplitude.

While the central concept of the wavefront splitting apodization method is simple, a variety of subtle factors must be analyzed and understood before devices employing it can be

designed. For example, one must look at how fields from the split diffractive elements interfere at various positions across the output plane. The phase difference does not remain constant. Ordinarily, it is the variation in relative phase of rays hitting various points on the diffractive element that determines the overall profile of the output spot. One finds that the split wavefront apodization method remains viable when this and other effects are incorporated into the analysis.

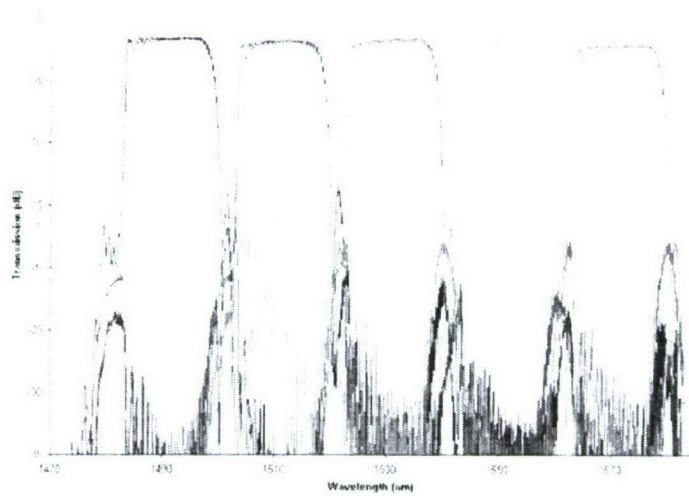


Figure 24. Five-channel CWDM mux apodized with the split contour method

We have designed and fabricated a five-channel CWDM mux unit with HBRs apodized using the split wavefront approach. The throughput of the mux is shown in Figure 24.

Generally speaking the mux performance is good. The insertion loss for all five channels (fiber-to-fiber) is better than about 2.5 dB. The polarization-dependent loss (not shown) is less than 0.2 dB. The passband wings fall off rapidly as a result of the split wavefront apodization. There are two anomalies. First, there is out-of-band cross talk (the peaks between the channels). Second, there are ripples on the passband.

The out-of-band crosstalk has been identified by modeling to result from a spatial spreading of the output spot consequent to introducing segments into the diffractive elements. Output ports were spaced at a distance that provided isolation for full contour output spots. This problem can be solved simply by increasing the spatial separation of ports on the output plane.

More problematic is the ripple within the passband. Our detailed Fresnel simulations of the structure do not reproduce it. Physically it appears to be a Fabry-Perot effect involving a reflection from the front end of the HBR and the designed operating point within the HBR, which gets deeper as the wavelength gets longer. Such an interference effect would produce the chirped passband ripple observed. We are speculating that some sort of impedance mismatch has been created within the planar waveguide at the front end of the HBR. In light of the

otherwise excellent performance of the split wavefront apodization method, it appears that more effort is warranted to understand and hopefully eliminate the ripple effect.

It should be noted that in a second wafer, designed to have lower reflectivity, the passband ripples do not appear (see Figure 25). The absence of ripples in devices from the low reflectivity, single-core wafer support the notion that some discontinuity associated with the multi-core waveguide (the second layer starts at the front of the HBR) may cause a broad band reflection. On the other hand, similar reflections are not found with other apodization methods. We continue to work to understand this feature.

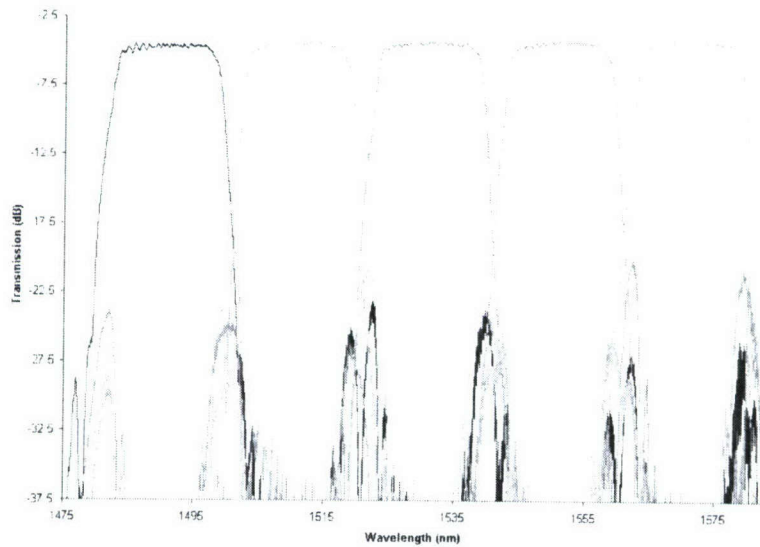


Figure 25. Five-channel HBR mux with split apodization implemented in a weakly reflecting waveguide geometry.

### Chromatic Dispersion in HBR CWDM Multiplexers

In initial evaluations of the performance of LightSmyth integrated CWDM multiplexer, potential customers have expressed concern over the chromatic dispersion produced by the device. Apparently, it is widely believed that grating-type devices exhibit unacceptably large chromatic dispersion. In response to this concern, we undertook a theoretical and experimental program to determine the chromatic dispersion properties of the HBR-based CWDM mux. We first describe theoretical modeling results which show that the LightSmyth device has low chromatic dispersion and we explain why.

Optical devices typically display chromatic dispersion. Chromatic dispersion physically corresponds to the presence of a wavelength dependent optical path length within the device. A wavelength dependent path length may arise from an intrinsic wavelength dependence of refractive indices, a wavelength dependence of waveguide propagation parameters, or a wavelength dependent physical path within the device. The latter is relevant to the HBR-based multiplexers. Chromatic dispersion is undesirable because it leads to a distortion of the temporal

profile of data signals propagating through the device.

HBR-based, integrated, silica-on-silicon multiplexers contain a chirped retroreflective diffractive structure (grating). The presence of chirp in the diffractive structure means that signals experience a wavelength-dependent physical path as they move between input and output ports. The gratings are oriented with their blue end toward the input so redder signals see a longer physical delay. The gratings are about 2.7-mm long and are chirped over a reflection bandwidth of about 15 nm. The maximum physical path difference is thus 5.4 mm and with an index of refraction of 1.45, the maximum optical path difference is 7.8 mm. In terms of delay, this corresponds to 26 ps. Thus we estimate crudely that the chromatic dispersion (delay/unit bandwidth) should be about 1.7 psec/nm. This is a very small value of chromatic dispersion and would lead to negligible signal distortion even at 40 Gbit/sec transmission rates.

We have performed a detailed mathematical simulation of the chromatic dispersion expected in grating structures modeled after those used in our multiplexers. The expected optical delay as a function of wavelength is shown in Figure 26 and the expected chromatic dispersion is shown in Figure 27.

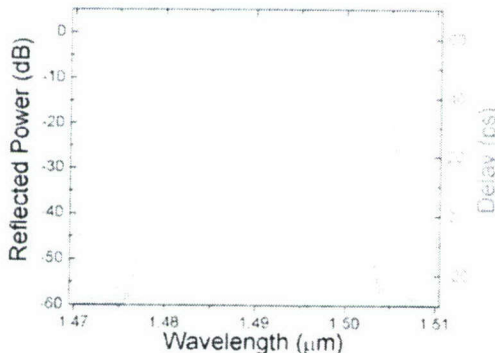


Figure 26. Wavelength dependent delay and reflection profile.

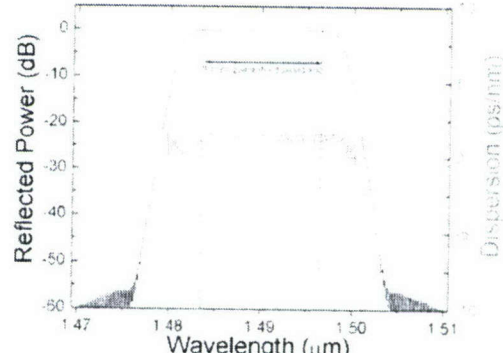


Figure 27. Chromatic dispersion (ps/nm) and reflection profile.

The detailed calculations of Figures 26 and 27 agree very well with the crude estimates given in the previous paragraph confirming that the chromatic dispersion of the integrated holographic multiplexer devices is very low and fully consistent with needs of even the most demanding communication systems.

It is interesting to try to understand why many workers in photonics have come to see large chromatic dispersion as a typical feature of grating-based devices. The most commonly utilized grating devices are fiber gratings. In fiber gratings, the diffractive structure is formed through Ultraviolet-induced refractive index changes. Achievable refractive index changes are typically less than  $10^{-3}$ . The refractive index contrast in the etched integrated holographic gratings being developed in the present Phase II SBIR are approximately 2 orders of magnitude larger. It

follows that fiber-grating-type devices configured to perform the same filtering function as an integrated holographic device would have to be roughly two orders of magnitude longer, producing physical path changes and therefore the chromatic dispersion roughly two orders of magnitude larger. It would appear that it is not grating structures per se that are plagued with high chromatic dispersion, but rather grating devices implemented with low refractive index contrast – where low means  $\Delta n < 10^{-3}$ . This result is made even more compelling by noting the thin-film filters are essentially grating devices as well, but operate with quite high refractive index contrast (order 0.5). Thin-film filter devices are viewed as relatively low in chromatic dispersion.

We have experimentally determined the chromatic dispersion properties of our HBR CWDM mux units. In Figure 28, we reproduce the calculated chromatic dispersion for one channel of a HBR-based CWDM multiplexer implemented with a standard 2.7-mm length and 13-nm operational bandwidth.

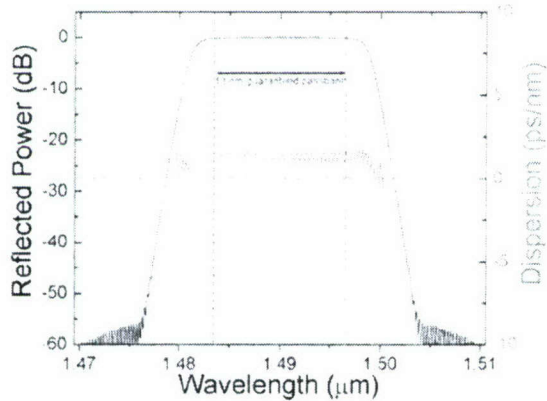


Figure 28. Wavelength dependent chromatic dispersion and reflection profile.

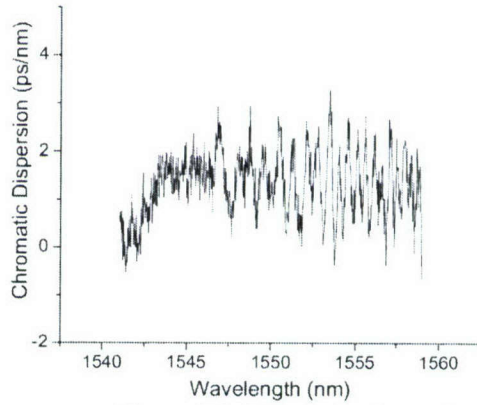


Figure 29. Measured chromatic dispersion (ps/nm).

The chromatic dispersion is approximately 2 ps/nm with spikes to about 3 ps/nm. In Figure 29, we present actual measurements of chromatic dispersion for a fabricated device. The center

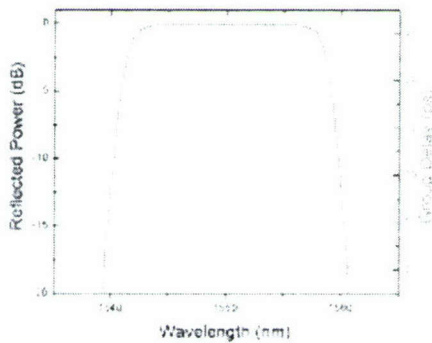


Figure 30. Calculated group delay versus wavelength

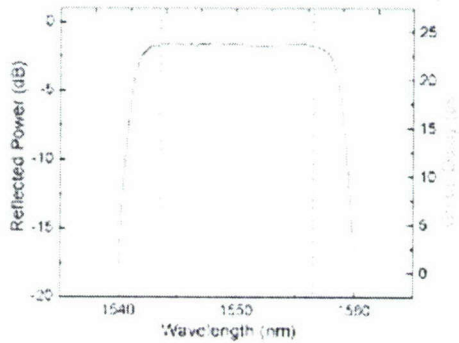


Figure 31. Measured group delay versus wavelength

wavelength for the filter actually measured (1550 nm) differs from the value used in the simulation (1490 nm); however, bandwidth and other physical properties were identical. Measurement agrees with theory indicating that the device chromatic dispersion in the approximate range of  $2(\pm 1)$  ps/nm.

At 40 Gbit/sec, the temporal distortion expected is thus about 0.6 ps. Considering the 25 ps bit duration, it is clear that the distortion is negligible. This remains true even at 100 Gbit/sec where the distortion is about 1.5 ps and the bit duration is 10 ps. At more popular bit rates of 10 Gbit/sec and lower, the device chromatic dispersion is practically non-existent.

In Figure 30, the calculated group delay versus wavelength is presented superimposed over the passband of the filter. In Figure 31, measured group delay versus wavelength is presented. Overall, agreement between calculation and measurement is excellent and demonstrate that chromatic dispersion is not a problem for HBR-based CWDM multiplexers even up to the 100 Gbit/sec level.

### **Impact of Waveguide Non-Uniformity**

#### Measurements

In Figure 32, we display the passbands of various channels in an HBR-based CWDM multiplexer. The device studied has 5 channels. It can be seen in Figure 32 that the mux has low overall insertion loss and that the increase in insertion loss from the first (bluest) channel to the last channel is small. The device in Figure 32 is essentially of product quality. Note that the bluest channel occurs physically first within the device while later (redder) channels are placed successively deeper into the device. The physical path within the device increases from left to right (blue to red) of the displayed channels.

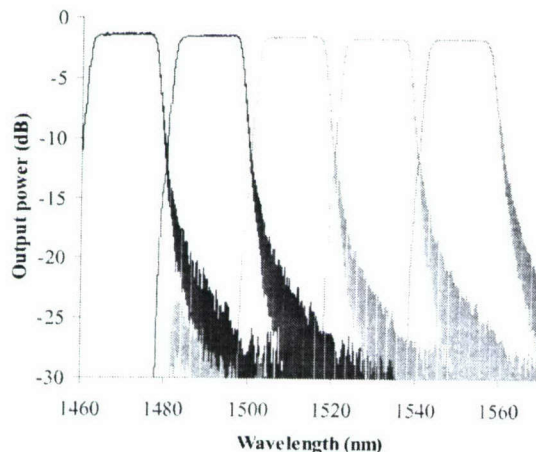


Figure 32. 5-channel CWDM mux fabricated with mostly uniform films and etch depth.

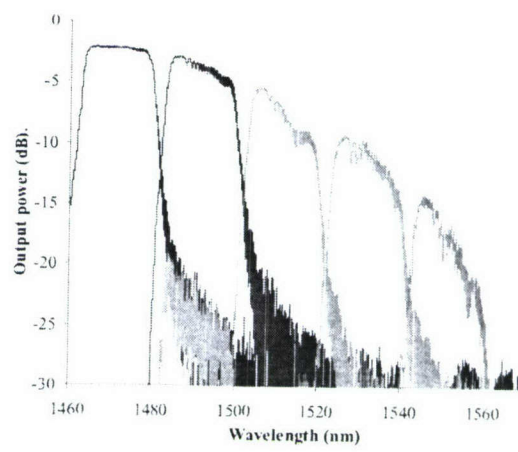


Figure 33. 5-channel CWDM mux exhibiting effects of film and etch inhomogeneity

In Figure 33, a 5-channel mux of a similar design as that of Figure 1 is shown. It is seen that the insertion loss increases from left to right among the channels which is equivalent to saying that

insertion loss increases with signal path length within the device. Without additional information, the data of Figure 33 could be interpreted to mean that the diffractive structures or the waveguide itself were lossy. We have conducted extensive analysis of the device including slicing it at various positions allowing light to be injected from various positions and allowing measurement of output directed signal beams in non-standard directions and positions. We found a very surprising result. For the device of Figure 33, we found that the outbound signal beams were defocused and spatially deflected from their design output configuration. The large increase in insertion loss shown in Figure 33 arises not because of energy loss within the device, but rather from a steering and defocusing of output signal so that it does not efficiently enter the output channel waveguides that route signal to the edge of the chip.

On analysis, we conclude that the most likely cause of this effect is either a non-uniformity of the waveguide index or a non-uniformity of the grating etch – which introduces indirectly a spatially varying index. Etch depth non-uniformity leads to waveguide index non-uniformity because the etched grating trench is filled with a material of different bulk index than the grating substrate leading to a local average material index that depends on etch depth. The steering and defocus result from different types of effective waveguide index non-uniformity. A linear ramp in index across a signal beam wavefront leads to beam steering. Random index fluctuations across the signal wavefront lead to defocusing.

Fortunately, from Figure 32 it is clear that proper foundry fabrication control can produce waveguide grating structures having sufficient uniformity to provide highly effective coupling of the output signal beams into their design output channel waveguides.

It is interesting to note that defocus/beam steering has only been observed when the slab waveguide has a dual layer structure. At the present time, we cannot tell whether it is the addition of the second layer itself that can cause the problem or whether it is etch depth variation in this higher index layer. To achieve high yield of the HBR mux products, control over the manufacturing process will have to improve beyond the level obtained in our Phase II work. Likely this will require a partnering, rather than pay as you go, relationship with the waveguide foundry.

### Compensating device geometries

We have investigated HBR design concepts that would tend to mitigate fabrication-induced inhomogeneities in waveguide refractive index. Such inhomogeneities can distort signal wavefronts and lead to increased device insertion loss since distorted signal wavefronts do not couple efficiently into single-mode output ports.

LightSmyth's approach in this is based on the notion that if signal modes can be made discrete rather than continuous as in a standard slab waveguide, it may be possible to keep signals in well-defined design modes with predictable wavefronts despite the presence of some level of fabrication-induced refractive index inhomogeneity. The idea is that with discrete and suitably differentiated modes, signals can follow inhomogeneity-induced mode variation adiabatically remaining within a single signal mode distorted only by local inhomogeneities. With continuous modes and non-adiabatic wavefront evolution, total wavefront distortion accumulates from the

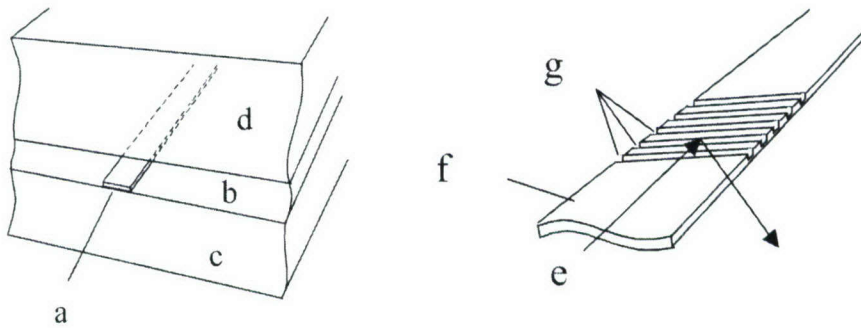


Figure 34. a) strip of grating material, b) core of slab waveguide, c,d) cladding material, c) input signal path, f) grating material guide, g) diffractive lines active to filter, focus, redirect

effect of all inhomogeneities experienced by the signal. We have devised an approach that translates these general conceptual ideas into simple more effective HBR devices. Multiple advantages of the design innovation accrue including greater lateral compactness as well as robustness from fabrication imperfections.

The basic approach is to create a waveguide within the standard slab waveguide (see Figure 34). Signals are weakly bound to a central core guide (a) and redirected and focused by diffractive lines (g) etched into the core guide into modes that propagate off to the side to output ports. As shown in Figure 35, the output direction may also have a stripe of guiding material.

In Figure 34, signals diffracted by etched diffractive lines in the guiding stripe (within the overall slab waveguide core) propagate via the continuum of slab modes once they are deflected by the diffractive lines. Generally, the lower refractive index material comprising the regular core layer is found to be more homogeneous than the grating material stripe (needed to provide high grating reflectivity) and so establishment of discrete propagation modes to preserve wavefront is not entirely necessary for signals propagating in the lower-index single-core region. The input signal is transversely bound to the higher index grating material stripe and should, in the presence of some classes of inhomogeneities, adiabatically follow mode evolution as it follows the stripe. Additional sections of diffractive lines selecting different wavelengths and focusing to different output ports can be placed in series along the guiding strip.

In Figure 35, a second grating material stripe is placed between the diffractive lines on the first guiding stripe and a design output port. In this case, inhomogeneities in the slab waveguide layer can be decoupled from signal wavefront perturbations also. Signals may be coupled to output channel waveguides by judicious tapering of the grating material stripe.

In both Figure 34 and 35, the guiding stripes are 10-100 microns wide so that each diffractive line produces a reasonably directional output signal. This prevents a wide spectrum of signals from being diffracted from the grating structure. This is important since diffraction over a wide bandwidth would introduce unwanted loss. The wide diffractive lines make the grating act as a volume hologram rather than a simple surface-type grating. Volume holograms preserve k-vector in multiple dimensions whereas surface gratings preserve only the k-vector

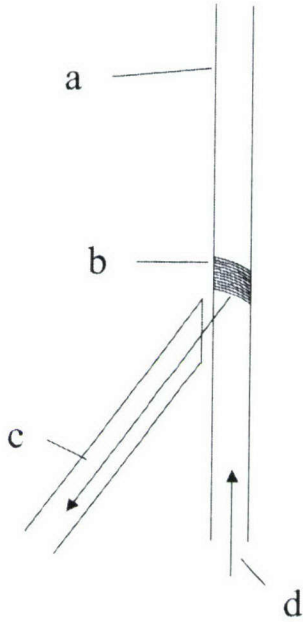


Figure 35. Grating guided signals. a) input stripe of grating material, b) diffractive lines (focus, filter, redirect), c) output stripe, d) input signal direction

component perpendicular to the grating lines. In the latter case, every wavelength can be diffracted. In the former case, only certain wavelengths can be diffracted.

Simulations and analysis of grating guided structures indicate that they do provide mode discreteness as needed to eliminate wavefront distortion otherwise introduced into slab waveguide bound signals by fabrication inhomogeneities.

We have simulated the impact of a spatial index variation, mimicking the size and magnitude expected from fabrication imperfections, on grating-guided and freely propagating signal modes. In the grating-guiding case, a model system comprising a 40 micron wide guiding strip, 0.5 microns deep, with index 1 percent above the 1.4565 index slab guiding layer was examined. Cladding layers had index 1.4457. A spatial index variation was introduced within the grating guiding layer. Within a region 15 microns wide and 2000 microns long, the index was decreased from the standard guiding layer value of 1.4728 to 1.4703. The perturbed region, modeling, for example, a dopant variation during manufacture, was tapered at both ends.

In the pure slab waveguide case, where the signal freely propagates within the plane of the slab, the same spatial index perturbation is introduced. In this case, the slab waveguide has grating material everywhere (i.e. the slab waveguide has two layers with the grating material layer perturbed by the shape described above). A freely propagating signal within the slab guide is made incident on the perturbation from the same direction as the grating-guided signal (i.e. from the perturbation's end).

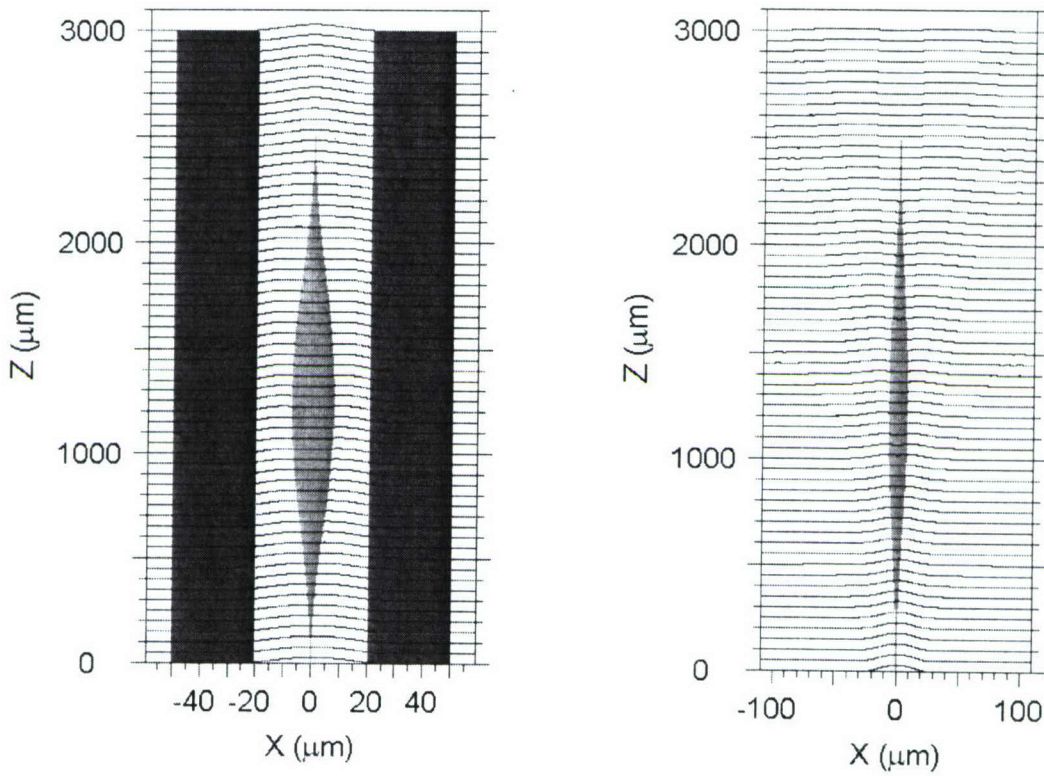


Figure 36. Profile of signal mode as a function of propagation depth,  $z$ , into a spatial region containing a refractive index inhomogeneity (thin tapered region at center of each plot). The left plot refers to a grating-guided signal and shows that the signal mode adiabatically propagates through the index defect region. The right plot shows that the same index inhomogeneity causes a permanent wavefront alteration in a signal freely propagating in a slab waveguide.

To determine the extent to which the spatial index perturbation coupled energy out of the signal mode, both grating guided and freely propagating fields were projected onto their forms obtained from models with no index perturbation. In other words, signals exposed to the perturbation were projected onto their original modes after propagating past the perturbation. It was found that the grating-guided signal retained approximately 95% of its original energy while the freely propagating signal retained only 77% of its energy in the original mode. These simulations were performed using the beam propagation method. Results confirm that the signal mode can be preserved in the face of local index perturbations by introducing a discretization into the propagating mode structure. In our case, the discretization is introduced by allowing grating material to guide the signal.

In Figure 36, the wavefront of a signal propagating through an index perturbation as described above is shown. The left plot shows the adiabatic propagation of the signal past the perturbed index region. As stated above the power remaining in the original guided waveguide mode remains 95% after the signal has past the index inhomogeneity. The right plot shows the permanent distortion of the freely propagating signal wavefront. Only 77% of the signal power remains in the original signal mode. In physical devices, the regions of perturbed index are

unpredictably positioned and in pure slab environments lead to the cumulative degradation of the originally intended signal wavefront. Such degradation may lead to major loss when the signal mode is routed off chip into a signal-mode transport means. In the case of grating guiding, which retains many of the flexible routing and signal control properties of the pure slab design, signal wavefront integrity is substantially less degraded indicating that pathways to high yield manufacturing are indeed available.

It is not necessary that the guiding structure used to discretize the slab waveguide modes is the grating layer material. A rib in the lower cladding or the addition of a dedicated material layer may also provide for mode discretization and therefore mode stability. Use of a dedicated structure for mode definition has the advantage of decoupling grating reflective strength from mode definition parameters. Generally, laterally defined modes should be as wide as possible so that the diffractive devices have narrow output diffraction angles.

### **Properties of HBR-based multiplexers in Silicon-on-Insulator Formats**

We have analyzed the implementation of Holographic Bragg Reflector filters and multiplexers in multimode waveguides based on the Silicon-on-Insulator (SOI) platform. SOI offers simpler and more cost-effective fabrication than the silica-on-silicon planar lightwave circuit platform as well as full CMOS compatibility.

Distributed diffractive structures such as holographic Bragg reflectors can be implemented as single or multimode solutions in the SOI platform. At typical telecom wavelengths of  $1.5\text{ }\mu\text{m}$ , single-mode solutions require waveguides to have core thicknesses of about 200 nm. Extraordinarily strong grating coupling can be achieved in highly confined single-mode waveguides. The strong grating interaction and tight confinement of SOI-based single mode distributed diffractive structures make possible highly integrated CWDM filters with very small footprints. On the other hand, the fundamental mode profile in a single-mode SOI waveguide is significantly different from that of a typical telecom fiber. This makes coupling an optical fiber to an SOI waveguide with low loss a challenging proposition.

HBRs may also be implemented in wider-core multimode SOI waveguides, which simplifies the coupling to outside standard telecom fibers. Gratings in multimode guides have multiple resonances at different wavelengths that arise from the coupling between the various horizontal modes. Device designs need to account for this effect so as to avoid undesirable losses. Here, we performed detailed analysis of the implementation of HBRs in SOI weakly multimode waveguides.

A key figure of merit in the design of Holographic Bragg reflectors is the available per-facet grating reflective strength since it determines the overall available reflective bandwidth for a given device length. The per-facet reflective strength depends in detail on the modal overlap of the resonant input mode with the grating as well as the grating's index contrast. We have explored the dependence of the grating strength on the core diameter of the SOI waveguide for fixed grating depth and set index contrast to determine the feasibility of a CWDM filter in SOI. The grating depth was chosen to be 300nm, consistent with standard etch recipes and reliable trench fill. The index contrast was kept fixed by simulating a grating between the Si core and an upper

$\text{SiO}_2$  cladding. Rather than showing results for the per-facet grating strength itself, we translate the latter parameter into the length required to make a CWDM filter reflecting a bandpass of 15-nm about its center wavelength with less than 1 dB transmission loss.

Figure 37 shows a cross-sectional view of the SOI slab waveguide, including grating structure, used for simulation. The slab waveguide consists of silica upper and lower (BOX, i.e. buried oxide layer) claddings with thickness  $d = 1 \mu\text{m}$ .  $w$  denotes the silicon core total thickness which was varied (specific values are given in the figures showing results). The grating region was

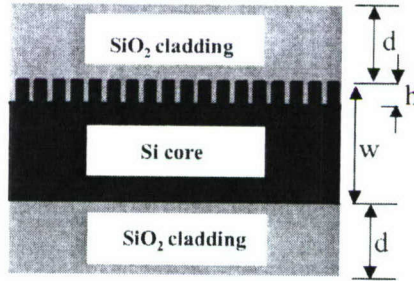


Figure 37. Cross-sectional view of silicon-on-insulator waveguide model used to study coupling strength and modal properties. The guide has 1- $\mu\text{m}$ -thick silica claddings.  $w$ , silicon core height;  $h$ , grating height (etch depth).

chosen to be  $h = 300 \text{ nm}$  deep, consistent with the 3:1 maximal aspect ratio that typically yields gap fill without voids. The grating is formed at the core-cladding interface by etching trenches into the silicon and subsequent deposition of silica or similar material of refractive index lower than the Si core.

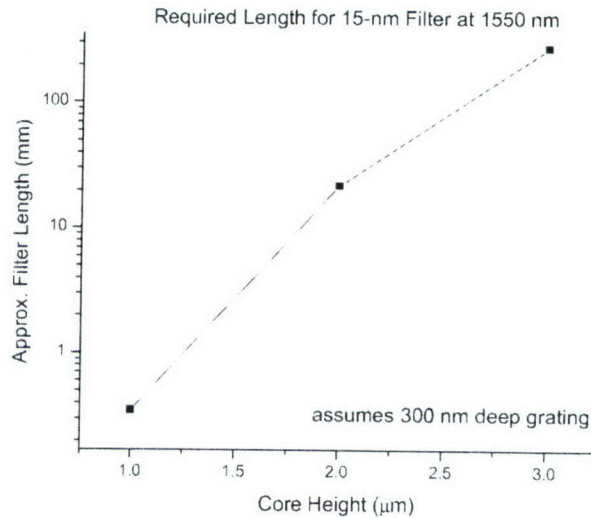


Figure 38. Required filter length versus height of Si core for single-channel CWDM filter with 15-nm passband. The grating etch depth is kept constant at 300 nm. Thinner cores yield strong coupling to the grating and thus reduced filter length.

Figure 38 shows the predicted required length of a CWDM filter reflecting a 15-nm window with acceptable insertion loss characteristics (<1 dB) as a function of core height. The results shown in Figure 38 are for coupling between input and output signals that are both in the fundamental mode of the waveguide. In Figure 38, a grating height of 300 nm was assumed. The results are further summarized in the table.

| Core Height h   | Approximate Filter Length (mm) |
|-----------------|--------------------------------|
| 3 $\mu\text{m}$ | 275                            |
| 2 $\mu\text{m}$ | 22                             |
| 1 $\mu\text{m}$ | 0.35                           |

For thinner cores the fractional overlap of the fundamental mode with the grating region increases which yields a shorter extinction length and consequently a shorter overall filter length. Based on the results of Figure 38 and the waveguide geometry shown in Figure 37 (etched grating in silicon filled with silica) a core height of 1 – 1.5  $\mu\text{m}$  would be desirable. Note that a passband roll-off within 1 nm requires an approximate minimum filter length of 1 mm owing to basic resolution principles, but for a CWDM design such steep roll-off may not be necessary. Based on the results of Figure 38 it is clear that a an SOI slab waveguide with 1  $\mu\text{m}$  thick Si

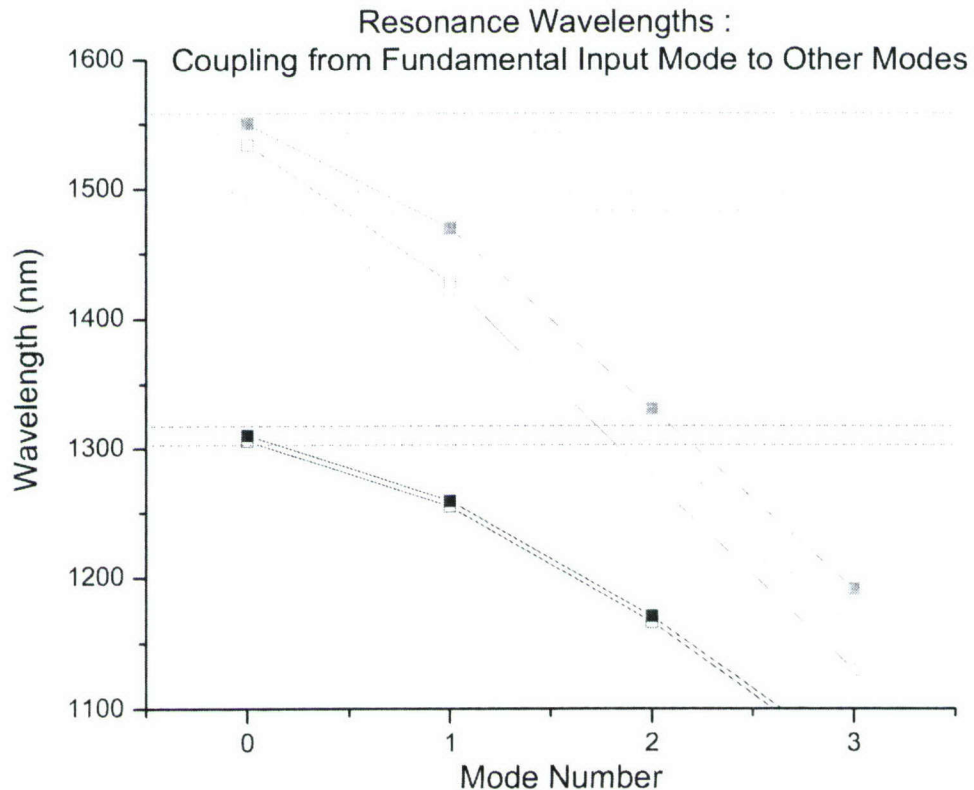


Figure 39. Plot of resonance wavelengths for gratings coupling the input fundamental to higher waveguide modes.

core can easily support an 8 or even 16-channel HBR CWDM multiplexer for device sizes consistent with the field size of DUV photolithographic stepper/scanners. Next, we consider the effect of the multiple modes present in the waveguide to further determine feasibility.

To this end, we show in Figure 39 the resonance wavelengths of gratings designed for three exemplary CWDM wavelengths of 1550 nm (top two lines), 1490 nm (middle two lines) and 1310 nm (bottom two lines) in a waveguide of 1  $\mu\text{m}$  core height. Due to the multimode nature of the waveguide each CWDM channel has multiple resonances at the wavelengths indicated by the symbols. For a given grating, the resonance wavelengths correspond to coupling of the fundamental mode (assumed to be the only input mode) to the other available modes (fundamental and higher). Coupling from the input fundamental mode to the fundamental output mode is indicated by the leftmost symbols in the graph. Solid symbols are for TE-polarization, empty symbols denote TM polarization. Shown as dashed lines are the passbands of the three CWDM channels. In the present simulation, the different resonant wavelengths for TE and TM polarizations are caused by form birefringence. In the results of Figure 38 the passband was designed wide enough to cover 15 nm for both polarizations.

It is clear that problems could arise when the fundamental-mode to higher-mode resonances of a given filter overlap the design passbands of filters for other signals. For example, resonances of the 1550-nm filter might fall within the passbands of the 1310nm or 1490 nm passbands. The 1550 nm grating would interact with fundamental-mode signals at those wavelengths, couple them to higher order modes and deflect them. Such interaction may lead to excess loss. This could be especially grave since the coupling from the fundamental to higher order modes is generally stronger than between fundamental modes. Appropriate spatial ordering of the HBR filters within the device can eliminate problems with fundamental-to-higher order mode scattering in some cases. Specifically, spatial ordering of the individual CWDM channel HBRs so that the bluest CWDM filters interact first with the multi-wavelength input can mitigate this potential problem.

Based on available reflective strength and assuming appropriate spatial ordering of the individual-channel HBRs an 8 or even 16-channel CWDM multiplexer based on multimode SOI waveguides appears fully feasible. Efficient telecom fiber to SOI waveguide coupling may be facilitated through the use of lateral tapers, as recently demonstrated by Lipson et al. at Cornell University or by diffractive input/output couplers like HBRs except optimized for interior/exterior mode coupling

We have also analyzed an alternate CWDM mux layout based on a multimode SOI waveguide wherein the etched grating trenches are filled with a material of refractive index higher than the silicon core, such as poly-Si or amorphous Si. Consequently, the grating region has an *average refractive index that is higher than the silicon waveguide core*. The advantage of this approach, as we shall see, is an increase in the grating's coupling strength even for relatively large Si core diameters. This should improve coupling to standard telecom fibers.

Figure 40 shows the alternate waveguide geometry that enables strong grating coupling, which allows filters to be short, while keeping the core height at 3  $\mu\text{m}$  and thus enabling more efficient

coupling to off-chip silica fibers. Here, rather than filling the etched Si with silica, a material with refractive index higher than silicon has been used (e.g., poly-Si, amorphous Si, or Ge-doped Si alloy). Since the resultant region has an average refractive index higher than Si, the mode field will tend to concentrate and be stronger in this region than in a Si/SiO<sub>2</sub> grating. Figure 41 and the corresponding table show the required length to make a 15-nm passband CWDM filter with acceptable insertion loss characteristics (<1 dB) as a function of refractive index of the new grating material for an Si core of 3 μm.

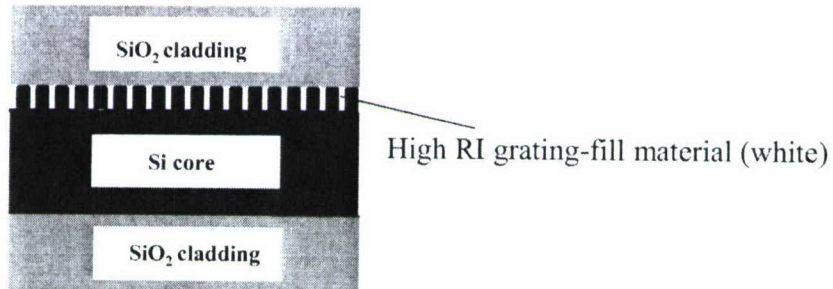


Figure 40. Cross-sectional view of alternative waveguide model. The grating is formed by etching 300-nm deep trenches into the 3-μm Si core and filling it with a material of higher refractive index than Si.

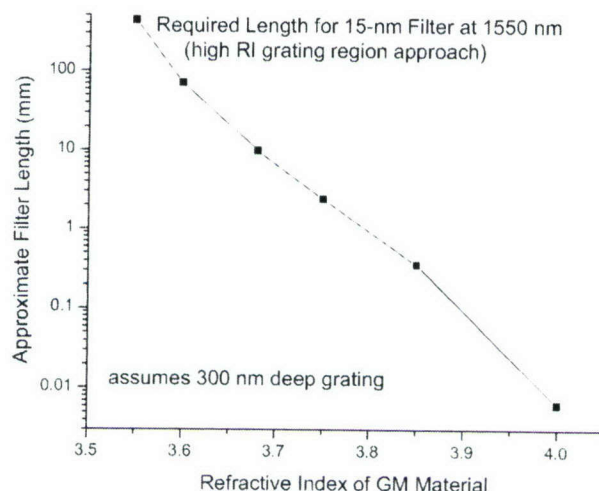


Figure 41. Required filter length for 20 nm passband versus refractive index of filling material. Grating height = 300 nm, Si core height = 3 μm. Higher refractive index yields stronger coupling to the grating and thus reduced filter length.

Based on the results of Figure 41, the waveguide geometry shown in Figure 40 would yield desirable filter lengths for a high-RI fill material with a refractive index around 3.8. Note that outside of the grating region, the higher refractive index material may be etched away to preserve taper solutions for effective fiber-to-waveguide coupling.

| Grating Fill Refractive Index | Approximate Filter Length (mm) |
|-------------------------------|--------------------------------|
| 3.55                          | 428                            |
| 3.6                           | 70                             |
| 3.68                          | 9.8                            |
| 3.75                          | 2.4                            |
| 3.85                          | 0.35                           |

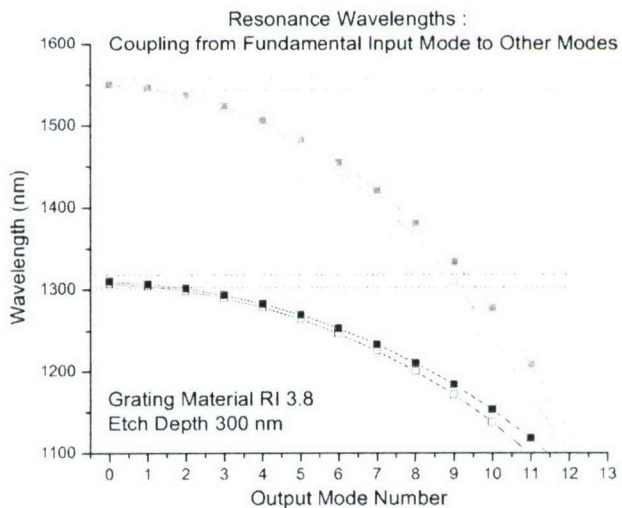


Figure 42. Resonance wavelengths of gratings at 1550 nm (red), 1490 nm (orange) and 1310 nm (blue). The Si core height is 3  $\mu\text{m}$ , the grating height is 300 nm. The grating was formed between Si and a material with refractive index 3.8. Solid squares, TE polarization, empty squares, TM polarization. 15-nm passbands are indicated by the dashed lines.

It is clear that an SOI slab waveguide with 3  $\mu\text{m}$  thick Si core and a grating filled with a  $n \approx 3.8$  refractive index material can easily support an 8 or even 16-channel HBR CWDM multiplexer.

Next, we consider again the resonance structure of three individual-channel CWDM filters (Figure 42). Two issues merit attention. First, certain resonances of a given CWDM filter corresponding to fundamental to higher mode reflection are seen to fall into the passbands of other CWDM channels. As discussed previously, this problem can be overcome by appropriate spatial stacking of the individual-channel HBRs. Second, multiple resonances of a given grating are also seen within the passband of a given CWDM channel. If the filters demux an input signal to a detector (essentially mode insensitive) the scattering to higher modes does not pose a problem provided that modal dispersion can be ignored for relevant bit rates and distances. However, in the reverse situation where a multicolor input signal from a laser array is to be muxed onto a single mode fiber, the coupling to higher modes that are not supported in the silica output fiber may lead to excessive and unacceptable losses.

### Conclusions and Comparison: Multimode CWDM in SOI

| Solution  | Pros  | Cons   |
|---|---|--|
| 1 $\mu\text{m}$ Si core height<br>300 nm deep grating<br>silica trench fill | - Acceptable coupling strength<br>- mm-scale total filter length                                      | - fiber-waveguide die coupling   |
| 3 $\mu\text{m}$ Si core height<br>300 nm deep grating<br>Hi RI trench fill  | - Acceptable coupling strength<br>- mm-scale total filter length<br>-good fiber-to-waveguide coupling | - only demux operation mux may have excessive loss due to coupling to higher modes |

### **Structuring HBR Diffractive Contours To Minimize Wavefront Aberration**

We describe the development of writing software that allows for the generation of HBR structures having aberration corrected wavefront transformation (imaging) capability. Prior design software and fabricated devices have utilized simple geometric diffractive line contours rather than true holographic contour definition.

Holographic Bragg Reflectors are so named for their potential to incorporate true holographic imaging into their structure. To do this, it is necessary to design a set of diffractive contours that faithfully represent the interference pattern between desired input and output signal waveforms. HBRs are designed on a computer and are not written by interferometric exposure. The computer design allows for the treatment of arbitrary input and output wavefronts whether or not such beams can be generated prior to device completion. Generally, signals in devices are not simple plane or spherical waves and rather represent solutions of the special boundary conditions present in the device. We have developed a design approach wherein the actual solutions appropriate to the waveguide structure are used to compute the HBR contour design. This tends to be a computationally bound process since thousands of individual contours typically need to be generated and sampled with points densely enough to allow interferometrically true fabrication.

If an HBR device is to be designed to image arbitrary wavefronts, it is necessary to actually calculate the full interference pattern. Geometric simplifications cannot generally be made. Our approach to the design problem then is to mathematically model the input and output beams and evaluate their sum as a function of position across the design dimensions of the HBR. The calculation occurs along straight lines across the HBR face and the family of points representing equal values of the interference pattern (e.g. maxima) is stored. Multiple straight slices of points are obtained and stored. A second algorithm is then employed that sorts the sampled points into contours. Contours are finally recorded as a sequence of straight segments each specified by its endpoints. Endpoints are spaced sufficiently close so that the straight line segment and the actual curved contour overlap to typically better than a fiftieth wave. The family of potentially hundreds of thousands or millions of segments are ultimately written by laser writer to a reticle

for DUV photolithographic fabrication.

In Figure 43(a), we show a set of points derived for a small HBR (size chosen for exposition purposes). In Figure 43(b), we show the points connected by segments. Both the points and the

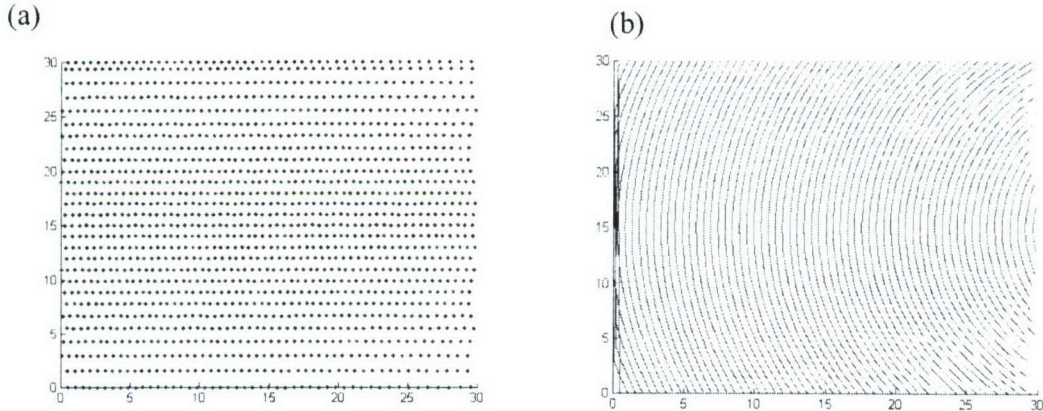


Figure 43. (a) A 30x30 micron HBR designed to accept a diverging input beam and focus it to an output port. The points represent equal value positions in the simulated interference pattern between the design input and output beams. (b) A sorting algorithm has been applied to collect points on the same contour together and link adjacent points with straight segments true to the contour to a settable accuracy.

segments are calculated using current versions of our HBR design software. In an actual HBR, there would typically be many thousands of lines.

The ability to design HBRs with full holographic function is important in efficiently mapping complex profile optical beams between various on-chip ports. Simple imaging devices (analogous to spherical optics) exhibit aberrations so that output signals are not properly mapped to target ports. We anticipate incorporating full holographic contour design in future devices.

### **Replication of HBR devices in PMMA**

We have investigated the replication of HBR diffractive structures, lithographically fabricated, via stamping in PMMA

An important objective of current and future optical communication component development is the creation of products that are low enough in cost to compete with electronic counterparts in application areas outside of long-haul and metro telecommunication links. Telecommunication links require parts with very long lifetimes, very high reliability, and very high performance. These constraints demand product solutions that tend to be too expensive for general purpose use. It is often true in consumer and other lower level applications that product life cycles are only a few years in duration and performance metrics are not nearly as stringent as in the telco environment. Thus substantially lower cost solutions can be entertained. In the present instance, we examine the use of polymer, PMMA, as substrate for a planar waveguide with the diffractive

structure created via stamping of a silicon substrate that carries a lithographically scribed pattern. The use of stamping opens a pathway to very low cost manufacture of HBR-based devices especially in the multi-mode CWDM area.

In Figure 44, we present a picture of a silicon master and a PMMA test piece on which the pattern of the master has been successfully transferred. The test diffractive structures contain curved lines and variable spacing as in the case of HBR structures. The test gratings have line densities of approximately 1000, 2100, and 4000 lines/mm. The middle line density corresponds to the value typically found in HBR multiplexer devices designed to work with 1.5 micron optical signals. All line densities were reproduced even the 4000 line/mm structure which required pattern transfer of features at the 125-nm level. Preliminary studies indicate that the replica diffractive devices have relatively high free-space diffractive efficiency (>50% of zeroth order, i.e. normalized to surface reflectivity) which in turn indicates that the replica has grooves that are approximately as deep as the original had mesas.

Proper replication requires careful control of PMMA and master temperature and stamping pressure. Successful replication was achieved in a convection lab oven within the temperature range 180° to 190°C, which is higher than typically used for thermoforming of PMMA (140° to 180°C). At lower temperatures, fine grating structures were not fully imprinted on PMMA. It was found that about 5 minutes of contact between the master and PMMA sample at the force of 20 N for 20 x 30 mm sample at 185°C is sufficient to obtain a quality imprint with all grooves fully imprinted. Higher temperature resulted in small bubbles in PMMA sample. Higher force simply deformed PMMA sample making it thinner and did not improve the imprint. It is possible that combination of lower temperature/higher pressure may reduce cycle time, which is very desirable for volume production.

Under most conditions, the PMMA frees itself of the master on cooling apparently because of differential heat expansivities of the materials. However, it remains desirable to identify a releasing agent that would ensure large area replication can be implemented without sticking

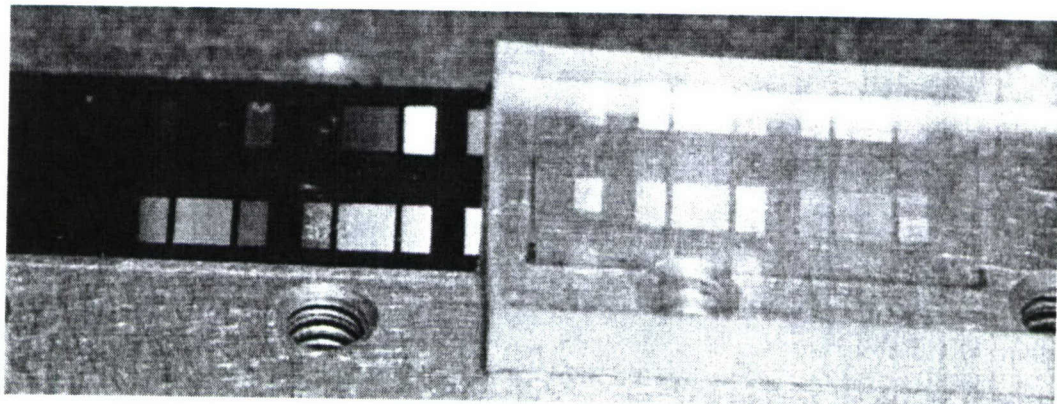


Figure 44. Left: Silicon master with lithographically scribed pattern. Right: PMMA test piece with diffractive pattern successfully transferred.

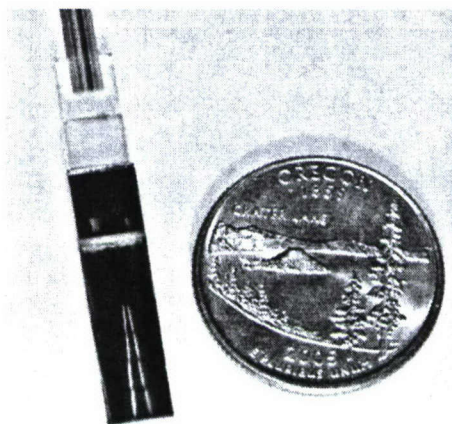
problems.

We conclude that low cost HBR devices can be implemented in PMMA guiding layers patterned via replication rather than higher cost lithography. Next steps would include application of pattern to thin PMMA layers supported by lower index substrates. This work will have to proceed in a post funding environment as the term of our development contract is essentially complete.

### Packaging Of HBR Mux Devices

We report on packaging solution for the final product. This includes development of optical assembly procedure and design of reliable housing for the optical assembly.

The packaging process involves preparation of the device die, active optical alignment of the die and the fiber array, and packaging of the optical assembly into the protective housing.



*Coarse WDM MUX die with fiber array by LightSmyth.*

#### Preparation of device die

Die preparation consists of the following steps:

- Dicing the wafer into device die. This step is done using standard semiconductor dicing machines. Use of sub-contractor is a cost-effective solution (dicing cost per wafer is \$100, or about \$0.3 /device).
- Attachment of top and bottom buffers (Fig. 45). This is required to increase the adhesion surface area to improve stability of the epoxy joint between the chip and a input/output fiber array. The buffers are made of glass or silicon (we chose glass) or about 1 mm thick glued to the top and bottom of the die.

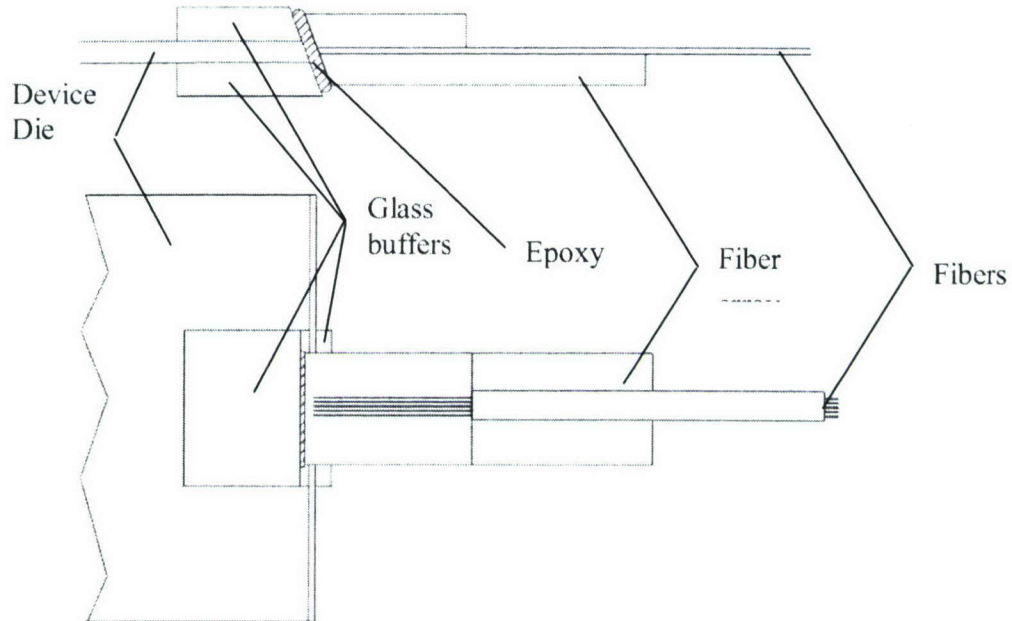


Figure 45. Optical assembly (top: side view; bottom: top view)

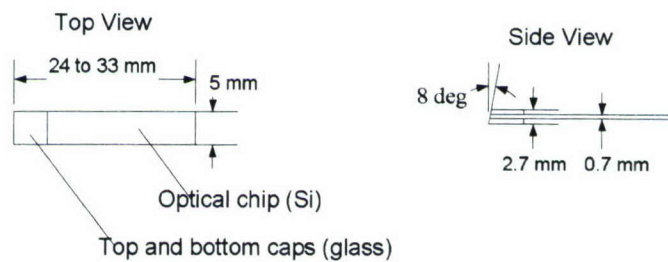


Figure 46. Attachment of top and bottom buffers (caps) and polishing of the die.

- Side polishing of the die (Fig. 46). Angle polishing is required to reduce Fresnel reflections from the interface between the optical epoxy/die and epoxy/fibers. Such reflections, if not reduced, adversely affect return loss of the device. For  $0^\circ$  polishing, such return loss may be below 35 dB, while for  $8^\circ$  polishing, return loss may be above 60 dB. For telecom applications, the required return loss is above 50 dB. The die with the buffers attached is polished in LightSmyth internal production facility using custom made polishing jig and commercial polishing machine. We achieved  $8^\circ$  angle polishing angle with accuracy of  $\pm 0.3^\circ$ . Fiber arrays are procured from a supplier and are pre-polished to  $8^\circ \pm 0.3^\circ$ .

- Surface preparation for epoxy application. This includes cleaning facets of the die and the fiber array with alcohol to ensure reliable adhesion.

#### Optical alignment.

It is important to optimize the relative position of the fiber and waveguide arrays to minimize the excess insertion loss caused by misalignment. An active optical alignment method is employed for LightSmyth devices when the position of the fiber array is adjusted based on an optical signal feedback. The sources of excess loss may be divided into several categories (Fig. 47): misalignment in X or Y direction (offset), separation along Z-axis (gap) and angular misalignment along angles Phi and Theta.

The die and the fiber array are both attached to positioning stages using quick-release clamps. Both stages have three degrees of translational freedom (XYZ), one stage in addition has three degrees of rotational adjustments (Roll, Pitch, and Yaw). Such arrangement allows for complete control over relative positioning of the die with respect to the fiber array enabling optimum optical alignment. Currently, the translations are performed manually and one optical assembly process takes about 15 min. Work is underway to use automated aligner to reduce the process time and costs.

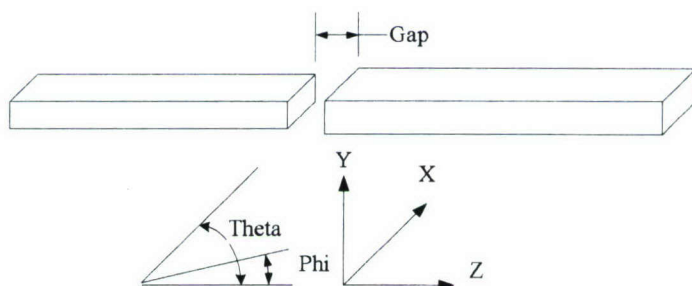


Figure 47. Parameters affecting excess loss in aligning a waveguide and a fiber (shown schematically). The waveguide on the left may be positioned with offset between the center of the waveguide and the fiber along OX and OY axis (offset), with certain distance between the ends of the fiber and the waveguide along OZ axis (gap) and tilted with respect to the fiber by an angle Phi (in YOZ plane) and Theta (in XOY plane).

Preliminary alignment is performed using visible laser source (HeNe) launched in the central fiber with separation between the fiber array and the chip of about 100 to 200  $\mu\text{m}$ . Then, epoxy is applied to the fiber array. The array and the die are brought to a separation of 20 to 30  $\mu\text{m}$  (controlled by divisions of the positioner), which is the optimum alignment distance. Larger distance would result in high insertion loss (Fig. 48), smaller distance may cause hard contact between the die and array during final alignment and epoxy cure, resulting in sharp increase in insertion loss as epoxy cures. The source is replaced by IR source at the wavelength of the channel multiplexed into the furthest output waveguide. Optical alignment is achieved by adjusting position of the fiber array monitoring and maximizing device output power. Because the spacing between the fibers in V-grooves and between the waveguides is controlled lithographically (250  $\mu\text{m}$ ), aligning the input fiber to the input waveguide and one output fiber to corresponding output waveguide results in alignment of the rest of the output waveguides,

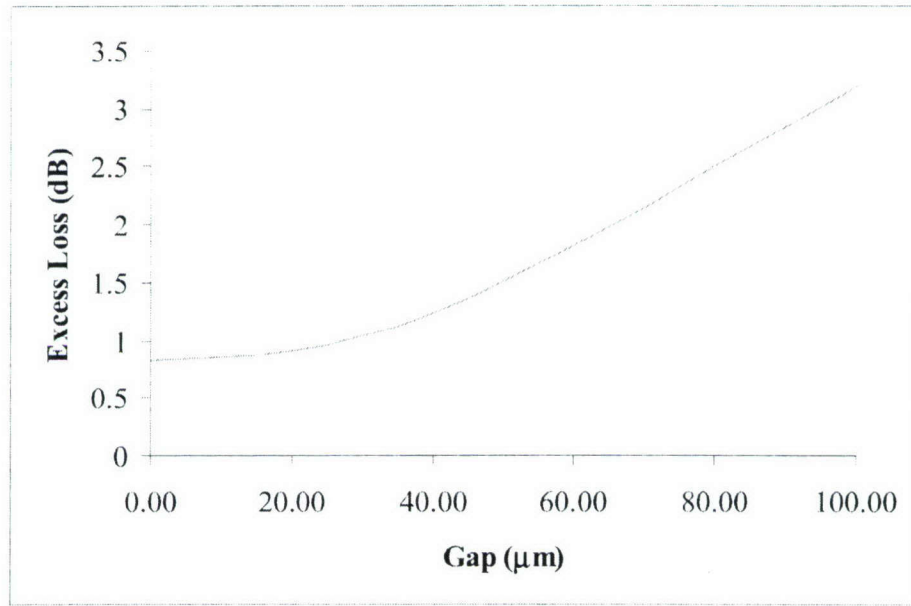


Figure 48. Insertion loss vs. Z-distance between fiber and waveguide.

reducing the need in additional alignment sources.

Sensitivity of insertion loss to displacement and misalignment (simulated data) is shown in Fig. 49 and 50, respectively. Spatial and angular resolution of the stage positioners (better than 0.25

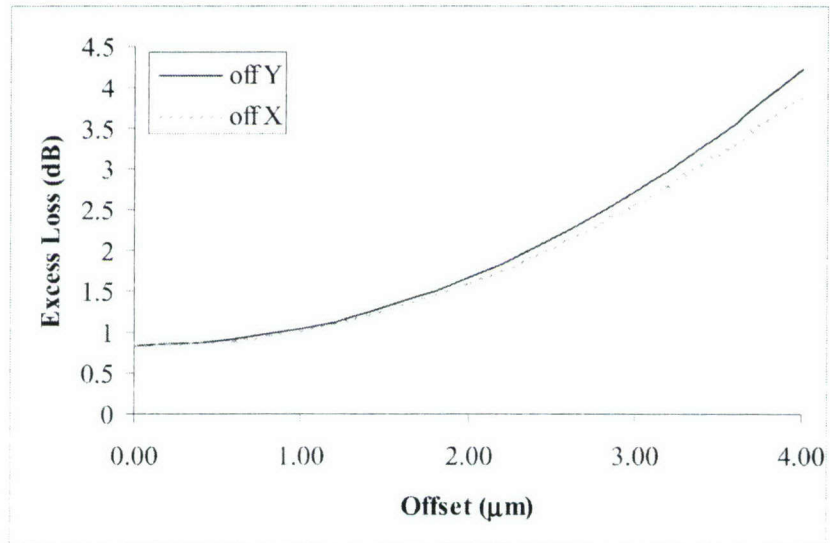


Figure 49. Excess alignment loss vs. X and Y offset between the center of the fiber and the center of the waveguide

micron and  $0.1^\circ$ , respectively) is needed to provide low-loss alignment. Estimated alignment loss achieved consistently is 0.2 dB.

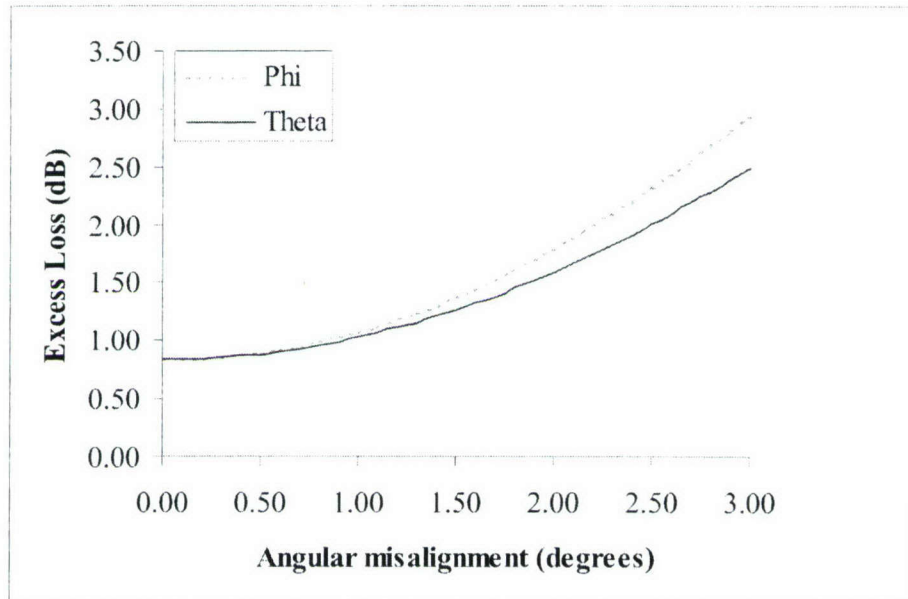


Figure 50. Excess alignment loss vs. angular misalignment

After achieving optimum optical alignment, the epoxy is cured. UV-cured epoxy was chosen as it does not create heat fluctuations that may adversely affect mechanical stability of the stages. The epoxy is designed to meet the reliability requirements of Telcordia GR-1221-CORE. UV spot curing system is used to deliver required UV dose. Curing time is 1 minute.

Insertion loss is monitored during the cure and after releasing the optical assembly from the quick-release clamps. Minimal change in insertion loss (<0.1 dB) during the cure and after the release indicates minimal stress in the epoxy joint. Larger change may indicate that the fiber array and the die were physically touching during the cure or that the separation between the die and the fiber array was non-uniform, creating misalignment as epoxy shrinks in volume during the cure.

Finally, insertion loss for all channels is measured against specification and, if necessary, the optical assembly is sent back for re-work. Alignment procedure developed by LightSmyth has 90% yield for the optical assembly step.

Optical assembly is placed in protective non-hermetic aluminum housing (Fig. 51). The housing is designed to apply minimum stress on the epoxy joint and protect the optical assembly from mechanical damages, shock and vibration. Due to the simplicity of the optical assembly (only single epoxy joint and single ribbon fiber), it was possible to design inexpensive and efficient housing. It is composed of a base, a lid, two pieces of foam and strain-relief boot (pre-inserted on fiber array assembly). Ribbon fiber is attached to the housing base with epoxy so that any pulling on the fiber would not be translated to the optical assembly inside of the housing. Strain relief

boot is designed to meet the reliability requirements of Telcordia GR-1221-CORE for side pull test. The die is sandwiched between the pieces of foam for protection against mechanical shock and vibration.

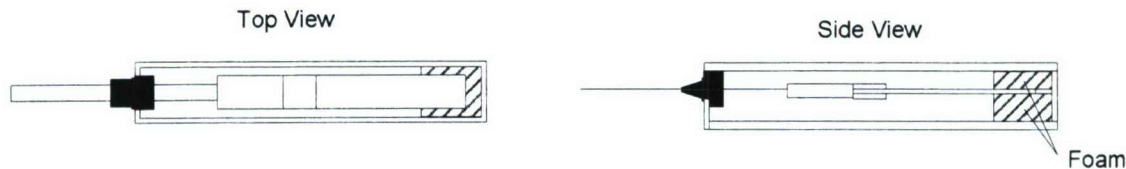
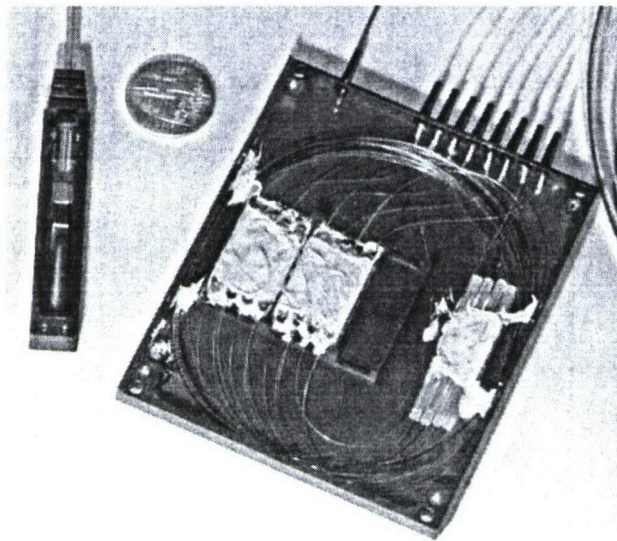


Figure 51. Die housing diagram

Completion of reliability testing of packaging used in telecommunication applications is an important step allowing marketing the product to a wider range of vendors. Initial reliability testing of the package (high temperature storage, low temperature storage and pull test) was successfully completed. Preparations for testing according to Telcordia GR-1209-CORE, including temperature cycling, accelerated aging (damp heat), temperature shock, mechanical shock and vibration are underway.



Comparison of CWDM produced by LightSmyth and competitor's product with similar performance based on discrete thin film filters. LightSmyth's integrated solution achieves 10x reduction in device size and number of sub-components dramatically reducing costs and increasing reliability.

## References

- 1. Integrated holographic filters for flat passband optical multiplexers, D. Iazikov, C. M. Greiner, and T. W. Mossberg, Optics Express 14, 3497 – 3502 (2006).**
- 2. Interferometric Amplitude Apodization of Integrated Gratings, T. W. Mossberg, C. Greiner, and D. Iazikov, Optics Express 13, 2419 - 2426 (2005).**
- 3. Submicron planar waveguide diffractive photonics, T. W. Mossberg, C. Greiner, and D. Iazikov, Proceedings from SPIE Conference on Integrated Optics: Devices, Materials and Technologies IX, Photonics West, paper 5728-23, pp. 203-211 (2005).**
- 4. Impact of high-resolution photolithography on integrated photonics, T.W. Mossberg, D. Iazikov, C.M. Greiner, Microlithography World, Vol. 14, #3, August/September 2005**

## 4 Channel CWDM Multiplexer / Demultiplexer

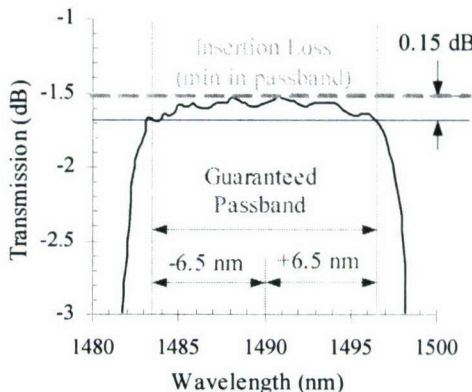
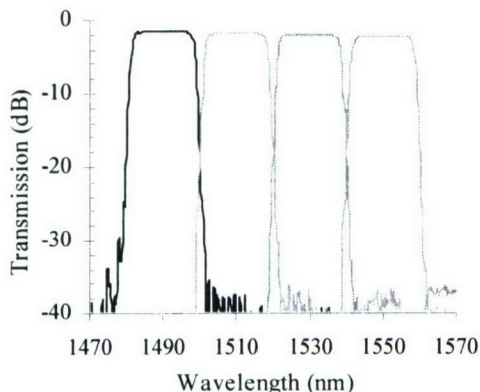
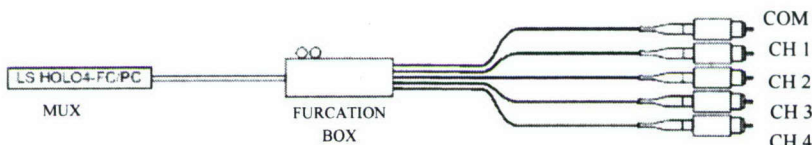
Crafting light for the Information Age

LightSmyth multiplexers/demultiplexers (mux/demux) incorporate breakthrough new technology to monolithically integrate thin-film-filter functionality into the robust silica-on-silicon planar waveguide format setting new standards for cost, performance, and footprint.

LightSmyth Coarse WDM mux/demux units are the first mainstream photonic devices employing nanophotonically engineered structures as their principal functional mechanism. Advanced engineering combined with reliable DUV photolithographic fabrication yield superior product.

### Key Features

- Monolithically integrated silica-on-silicon mux/demux engine
- Ultra-small footprint
- Low part count
- Low cost
- High performance
- Athermal operation
- All ports single-mode compatible

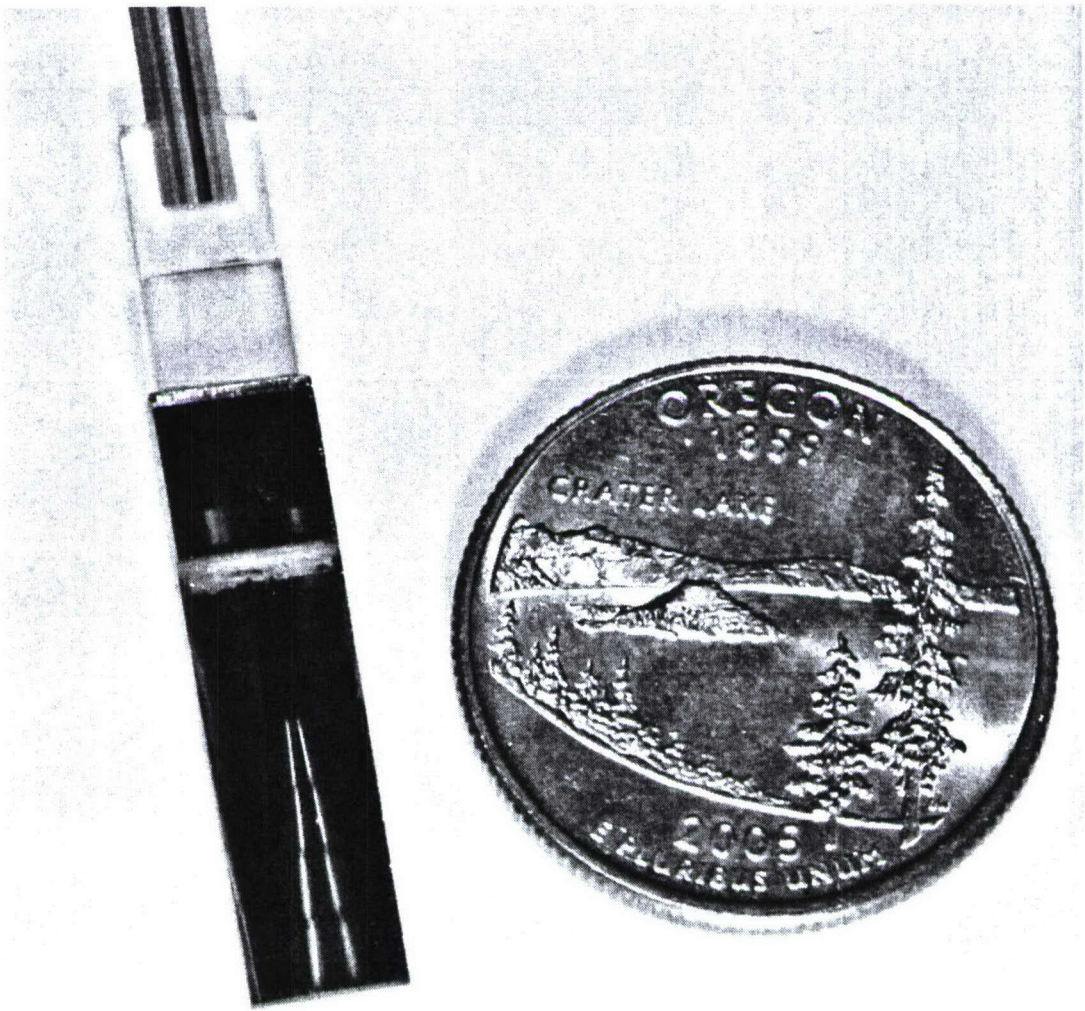


### Specification

| Parameter   | All channels                                      |         |
|---|---|---------|
| Channel central wavelength (CCW)  | 1490 nm, 1510 nm, 1530 nm, 1550 nm <sup>(4)</sup> |         |
| Insertion loss <sup>(1, 2)</sup> , connectorized device, excluding connector loss | Max   | 2.2 dB  |
| Passband to -0.3 dB level (symmetric about CCW)                                   | Min   | 13 nm   |
| Flatness <sup>(1, 2)</sup> (difference between max to min insertion loss)         | Max   | 0.3 dB  |
| Adjacent channel isolation <sup>(1, 2)</sup>                                      | Min   | 33.5 dB |
| Non-adjacent channel isolation <sup>(1, 2)</sup>                                  | Min   | 34.0 dB |
| Polarization dependent loss (PDL) <sup>(1, 2, 3)</sup>                            | Max   | 0.2 dB  |
| Optical return loss <sup>(1)</sup>  | Min   | 35.0 dB |
| Dimensions  | 12 x 12 x 65 mm                                   |         |
| Optical connector   | FC/PC, others available                           |         |
| Fiber type  | SMF 28  |         |
| Operating temperature range   | -40 to 85 °C                                      |         |
| Storage temperature range   | -40 to 85 °C                                      |         |

### Notes:

1. Defined as worst channel case over the entire operating temperature range and all input polarization states.
2. Defined within -0.3 dB level guaranteed passband.
3. PDL is defined as min/max insertion loss difference at any wavelength in the passband over all input polarization states.
4. Custom passbands and channel central wavelength from 1260 nm to 1610 nm available.



LightSmyth Technologies announces the world's first fully integrated, single-mode compatible, coarse WDM (CWDM) multiplexer. Based on LightSmyth's patented nanophotonic filtering technology, the unit breaks records for size, part count, and cost while exceeding customary performance levels. LightSmyth integrated CWDM multiplexer units are passively athermal and polarization insensitive to 0.2 dB. LightSmyth's new integrated CWDM multiplexer is based on the silica-on-silicon planar waveguide format, requires chips of only 1 cm<sup>2</sup>, and is the first photonic device to productively harness the Deep UV photolithographic patterning tools utilized in state-of-the-art electronics. LightSmyth's underlying filtering technology may also be referred to as integrated holographics (see Laser Focus World October 2004, pp. 73 – 76). Competing CWDM technologies utilize gratings or free-space thin-film filters. Grating devices can be integrated but require multimode outputs to produce low-loss flat-top passbands. Thin-film filters support flat-top passbands but cannot be monolithically integrated. LightSmyth's new diffractive nanophotonic filtering engine uniquely and powerfully combines the integrability of gratings with the functionality of thin-film filters.

## 8 Channel CWMD Multiplexer

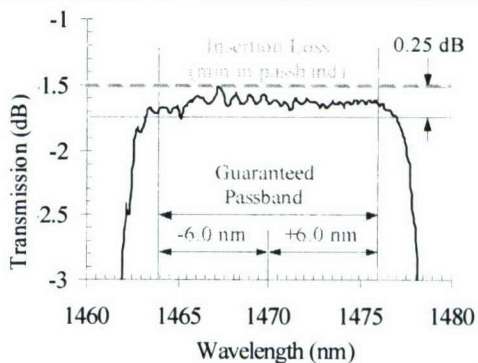
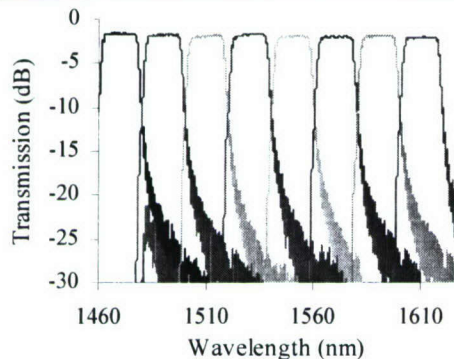
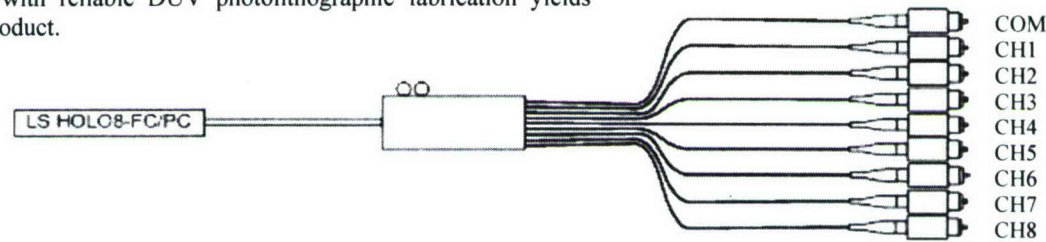
Crafting light for the Information Age

LightSmyth multiplexers (mux) incorporate breakthrough new technology to monolithically integrate thin-film-filter functionality into the robust silica-on-silicon planar waveguide format setting new standards for cost, performance, and footprint.

LightSmyth Coarse WDM mux units are the first mainstream photonic devices employing nanophotonically engineered structures as their principal functional mechanism. Advanced engineering combined with reliable DUV photolithographic fabrication yields superior product.

### Key Features

- Monolithically integrated silica-on-silicon mux/demux engine
- Ultra-small footprint
- Low part count
- Low cost
- High performance
- Athermal operation



### Specification

| Parameter   | All channels  |          |
|---|---|----------|
| Channel central wavelength  | 1470 nm, 1490 nm, 1510 nm, 1530 nm, 1550 nm, 1570 nm, 1590 nm and 1610 nm |          |
| Insertion loss <sup>1,2</sup> , connectorized device, excluding connector loss    | Maximum   | 2.0 dB   |
| Guaranteed passband <sup>1</sup> (–0.5 dB level about channel central wavelength) | Minimum   | ± 6.0 nm |
| Flatness <sup>1,2</sup> (difference between max to min insertion loss)            | Maximum   | 0.5 dB   |
| Adjacent channel isolation <sup>1,2</sup>   | Minimum   | 15 dB    |
| Non-adjacent channel isolation <sup>1,2</sup>                                     | Minimum   | 25 dB    |
| Polarization dependent loss (PDL) <sup>1,2,3</sup>                                | Maximum   | 0.2 dB   |
| Optical return loss <sup>1</sup>  | Minimum   | 31.0 dB  |
| Dimensions  | 12 × 12 × 65 mm   |          |
| Optical connector   | FC/PC, others available   |          |
| Operating temperature range   | −40 to 85 °C  |          |
| Storage temperature range   | −40 to 85 °C  |          |

### Notes:

1. Insertion loss, guaranteed passband, isolation and optical return loss are defined as worst case channel over the entire operating temperature range and all input polarization states.
2. Insertion loss, flatness, isolation and PDL are defined within –0.5 dB level guaranteed passband.
3. PDL is defined as min/max insertion loss difference at any wavelength in the passband over all input polarization states.
4. Custom passbands and channel central wavelength from 1260 nm to 1610 nm available.